Synchronization between chloroplastic and cytosolic protein synthesis for photosynthesis complex assembly

Tomoya Fujita[1,2,15], Taisei Wakigawa[1,3,15], Naohiro Kawamoto[1], Yukio Kurihara[4], Yuu Hirose[5], Takashi Hirayama[6], Hirotaka Toh[1], Tomoko Kuriyama[4], Atsushi Hashimoto[7], Eriko Matsuura-Suzuki[1], Keiichi Mochida[8-12], Minoru Yoshida[7,13,14], Minami Matsui[4], and Shintaro Iwasaki[1,2,16*]

[1]RNA Systems Biochemistry Laboratory, RIKEN Cluster for Pioneering Research, Wako, Saitama 351-0198 Japan

[2]School of Life Science and Technology, Tokyo Institute of Technology, Midori-ku, Yokohama 226-8503, Japan

[3]Department of Computational Biology and Medical Sciences, Graduate School of Frontier Sciences, The University of Tokyo, Kashiwa, Chiba 277-8561, Japan

[4]Synthetic Genomics Research Group, RIKEN Center for Sustainable Resource Science, Tsurumi-ku, Yokohama 230-0045, Japan

[5]Department of Applied Chemistry and Life Science, Toyohashi University of Technology, Toyohashi, Aichi 441-8580, Japan

[6]Group of Environmental Response System, Institute of Plant Science and Resources, Okayama University, Kurashiki, Okayama 710-0046, Japan

[7]Chemical Genomics Research Group, RIKEN Center for Sustainable Resource Science, Wako, Saitama 351-0198, Japan

[8]Bioproductivity Informatics Research Team, RIKEN Center for Sustainable Resource Science, Yokohama 230-0045, Japan

[9]Kihara Institute for Biological Research, Yokohama City University, Yokohama 244-0813, Japan

[10]Graduate School of Nanobioscience, Yokohama City University, Yokohama 236-0027, Japan

[11]School of Information and Data Sciences, Nagasaki University, Nagasaki 852-8521, Japan

[12]Microalgae Resource Upcycling Research Laboratory, RIKEN Baton Zone Program, RIKEN Cluster for Science, Technology and Innovation Hub, Yokohama 230-0045, Japan

[13]Office of University Professors, The University of Tokyo, Bunkyo-ku, Tokyo 113-8657, Japan

[14]Collaborative Research Institute for Innovative Microbiology, The University of Tokyo, Bunkyo-ku, Tokyo 113-8657, Japan

[15]These authors contributed equally.

[16]Lead contact

[†]Correspondence: shintaro.iwasaki@riken.jp (S.I.)

Summary

Through symbiosis, subunits of chloroplastic complexes are encoded in distinct genomes in the nucleus and organelles. For plant cells to maintain the stoichiometry of subunits and respond to environmental cues, orchestration of the nuclear and organellar gene expression systems is an essential task. However, the mechanism maintaining chloroplastic complexes remains largely enigmatic. Here, we simultaneously assessed the translatomes of the chloroplast and the cytoplasm via ribosome profiling and revealed the differential mechanisms employed by these two systems to cope with acute light/dark transitions: in chloroplasts, translational regulation is employed, whereas in the cytoplasm, control of the mRNA abundance is employed. This strategy is widely conserved in land plants (*Arabidopsis* and the grass plant *Brachypodium*) and green algae (*Chlamydomonas*). The translational control in chloroplasts may be established on the basis of organelle symbiosis; the primitive chloroplast in Glaucophyta (*Cyanophora*) was found to have already acquired translational control, whereas cyanobacteria (*Synechocystis*) employ control of the mRNA abundance. Moreover, treatment with photosynthetic electron transport inhibitors indicated that reduced plastoquinones may trigger translational activation in chloroplasts. Our work reveals an early origin of coordination of chloroplast and nuclear/cytoplasmic gene expression upon light exposure.

Introduction

Most biological energy on Earth is supplied through photosynthesis. This reaction occurs in chloroplasts through the multiple protein complexes in plants (*1–5*). The photosynthetic apparatus is assembled from proteins encoded in two distinct genomes: the nuclear genome and the chloroplast genome (*6*, *7*). This complicated scheme is due to ancient cyanobacterial symbiosis and coevolution; some genes encoding subunits of the photosynthetic apparatus were transferred to the nuclear genome, whereas others are still encoded in the chloroplast genome. Ultimately, the subunits of the photosynthetic apparatus are translated in two distinct subcellular locations—the cytoplasm and the chloroplast stroma. A balanced supply of subunits from these two origins is crucial to proteostasis in plant cells, since excess free subunits or immature complexes can result in detrimental effects on cells (*8*, *9*). However, the mechanisms underlying the coordinated protein synthesis between the cytosol and chloroplast stroma remain elusive.

Oxidative phosphorylation (OXPHOS) complexes in mitochondria are faced with a similar challenge, also requiring the coordination of gene expression between the nuclear genome and the mitochondrial genome (*10–12*). In yeasts, the two distinct gene expression systems in the cytosol and the mitochondrial matrix are synchronized at the translational level to allow adaptation to respiratory metabolism (*13*). Although it is logical to hypothesize the presence of similar synchronization of gene expression between the cytosol and chloroplasts in plants to support their response to environmental cues, the presence of such a mechanism is unclear.

To investigate the cooperation of gene expression systems for the nuclear genome and chloroplast genome, we harnessed ribosome profiling, a technique based on deep sequencing of ribosome-protected RNA fragments (i.e., ribosome footprints) generated

by RNase treatment (*14*, *15*). We employed this strategy, which has been used for the simultaneous assessment of cytosolic and mitochondrial translation in mammals (*16–18*), for to monitor cytosolic and chloroplastic protein synthesis in land plants, green algae, and Glaucophyta. We found that upon environmental transitions between light and dark conditions, the supply of subunits for photosynthetic apparatuses aligned with the demands, i.e., a lower synthesis rate under dark conditions and a higher synthesis rate under light conditions. However, the mechanistic basis of this orchestration differed between the subcellular locations: regulation of the RNA abundance in the cytosol and regulation of translation in chloroplasts. On the other hand, in cyanobacteria, the evolutionary origin of chloroplasts, the RNA abundance is regulated, suggesting the emergence of a translational regulatory mechanism upon symbiosis. We also found that a reduced form of plastoquinone (PQ) produced by photosystem II (PSII) activates translation in chloroplasts. Our study provides fundamental insight into the synchronization of gene expression from two different genomes for environmental adaptation.

Results

Plant ribosome profiling simultaneously assesses translation in the cytosol and chloroplast stroma

Given that the subunits of the photosynthesis complexes in the thylakoid membrane are encoded by dual genomes, we inferred the presence of coordination between two gene expression systems. To monitor protein synthesis in both the cytosol and chloroplasts simultaneously, we performed ribosome profiling on *Arabidopsis thaliana* seedlings. To this end, we obtained whole-cell lysates containing both cytosolic and chloroplastic ribosomes (Figure 1A) (see the Materials and Methods section for details). The majority (88.5%) of the reads originated from nuclear genome-encoded mRNAs (i.e., cytoribosome footprints), while chloroplastic mRNA fragments (chlororibosome footprints) constituted a small but significant fraction (7.3%) of the reads (Figure 1B).

The lengths of ribosome footprints are determined by the sizes and conformational status of ribosomes and thus often fall into characteristic size ranges (*19–25*). As observed in other eukaryotes (*19*, *23*, *25*), cytosolic ribosomes showed two distinct peak sizes—short, ~21 nucleotides (nt); and long, ~28 nt (Figure 1C). These sizes represent the absence and presence of an A-site tRNA on the ribosome, respectively (*23*). On the other hand, the chloroplast ribosome footprint lengths were restricted to ~24 nt (Figure 1C). Notably, although earlier studies showed a wider distribution of longer footprints from chloroplasts (*26–30*), this observation may have been due to insufficient RNase digestion.

The presence of three-nucleotide periodicity in footprints ensures codon resolution in the data. Indeed, the meta-gene plots showed a periodic pattern of reads along the open reading frame (ORF) for both cytoribosome footprints and chlororibosome footprints (Figure 1D and 1E). This observation was further supported by discrete Fourier

transform calculations (Figure 1F and 1G). These data indicated that our libraries were qualified for simultaneous assessment of cytosolic and chloroplastic translation.

In our meta-gene analysis of chloroplast ribosome footprints, we observed the 5′ extension of the footprints around the start codon (Figure 1E), reminiscent of bacterial ribosome footprints (Figure S1A). The increased lengths of bacterial ribosome footprints around the start codon can be explained by the failure of RNA cleavage due to the RNA duplexes formed between the Shine–Dalgarno (SD) sequence in an mRNA and the anti-SD sequence in a 16S rRNA (*20*, *24*). Although SD/anti-SD base pairing facilitates translation initiation in bacteria (*31*, *32*), the importance for chloroplast translation has remained controversial (*33–40*). Our data suggested that the region upstream of the AUG codon, including the SD sequence, may interact with an anti-SD sequence in the chloroplast 16S rRNA.

Chloroplastic ATP synthase subunits are synthesized in proportion to the stoichiometry of the complex

Multisubunit complexes may contain each protein subunit in different stoichiometries. Imbalanced subunit synthesis leads to nonfunctional complexes or orphan proteins, which may have adverse effects and thus should be degraded (*9*). To reduce the cellular cost, cells synthesize protein subunits in proportion to the stoichiometry of the complex (*41–43*). The bacterial F_oF_1 ATP synthase, which consists of subunits at a stoichiometric ratio of 1:2:3:10, is a notable example (*41*). The synthesis of the homologous complex on the chloroplast thylakoid membrane is more challenging; the subunit proteins are encoded by genes that are not in the same operon, as they are in bacteria; are encoded in two genomes; and are translated in different subcellular domains.

Even with these difficulties, the subunits of the chloroplastic F_oF_1 ATP synthase are still proportionally synthesized, irrespective of the translation system (Figure 1H). A similar pattern of proportional subunit synthesis was suggested for maize, *Arabidopsis*, and *Chlamydomonas* via ribosome profiling (*27*, *44*, *45*). However, these studies did not consider the subunits translated by cytoribosomes. Here, we showed that dual translation systems coordinately control the supply of subunits.

Light-dependent synchronization of dual gene expression systems for chloroplastic multisubunit complexes

Since F_oF_1 ATP synthase is a component of the photosynthesis system, we investigated the dynamics of its synthesis rate during acute light-to-dark and dark-to-light transitions (Figure 2A). With reduced light exposure, we observed decreases in the footprints of both translation systems for F_oF_1 ATP synthase subunits (Figure 2B, left). Reillumination of the plant restored subunit synthesis (Figure 2B, left). Thus, the synchronization of the two gene expression systems adjusted to meet the demand for F_oF_1 ATP synthase in response to environmental changes.

However, strikingly, the mechanistic basis differed between the two gene expression systems. Simultaneous RNA-Seq analysis revealed drastic reductions in the levels of cytoplasmic mRNAs encoding F_oF_1 ATP synthase subunits under dark conditions and the restoration of their levels upon reillumination (Figure 2B, middle). Thus, the alterations in cytoribosome footprints (Figure 2B, left) originated predominantly from transcript availability. Consequently, the change in the "translation efficiency", a relative score indicating the over- or underrepresentation of ribosome footprints relative to RNA-Seq fragments, did not follow the changes in the footprint

(Figure 2B, right). In contrast, the changes in chloroplastic mRNA level could not explain the footprint dynamics upon light exposure (especially under dark conditions, when chloroplastic mRNAs were enriched, unlike footprint changes) (Figure 2B, middle). Rather, the translation efficiency was a major regulatory mechanism (Figure 2B, right).

In addition to F_oF_1 ATP synthase, the other photosynthesis complexes, including PSII, the cytochrome b_6f complex (Cyt b_6f), photosystem I (PSI), and the NADH dehydrogenase-like complex (NDH), are multisubunit assemblies that require gene expression via dual systems. Thus, we further extended our analysis to those complexes. Indeed, the subunits of all these complexes subunits showed essentially the same dynamics as F_oF_1 ATP synthase; the dark and light transitions induced synchronized subunit synthesis from the two gene expression systems, as evidenced by the ribosome profiling results (Figure 2C-F). RNA-centric regulation was dominant in the cytosol, whereas translation-centric regulation was mainly observed in chloroplasts.

Conservation of synchronization between dual gene expression systems

These observations led us to expand our analysis to include green lineages, such as *Brachypodium distachyon* (Figure S2), a model grass plant (*46*), and green algae *Chlamydomonas reinhardtii* (Figure S3). As was possible for *A. thaliana*, ribosome profiling of these species allowed us to monitor both cytosolic and chloroplastic protein synthesis, as evidenced by the 3-nt read periodicities (Figures S2A-G and S3A-G).

Both green lineages also exhibited environment-tailored protein synthesis for thylakoid membrane-embedded complexes, which was downregulated in the dark and restored in the light (Figure 3B-C), as observed in *Arabidopsis* (Figure 3A). Moreover, the modes of regulation were also conserved; protein subunits generated in the cytosol

were regulated at the RNA level, whereas chloroplastic subunits were regulated at the translational level (Figures 3A-C, S2I-M, and S3I-L).

Ribosome footprint analysis in *B. distachyon* may require additional caution. The nuclear genome of *B. distachyon* contains a large number of chloroplast gene duplications due to gene transfer (nuclear plastid genes) (*47*). Thus, the reads mapped to the chloroplast genome could also be assigned to nuclear plastid genes because of their high sequence similarity (Figure S2N). However, we assumed that the reads mapped to chloroplast transcripts predominantly represented chloroplastic translation because 1) the majority of the nuclear plastid genes were known to be pseudogenes (*47*) and 2) the footprints mapped to the chloroplast genome had different sizes than those mapped to the nuclear genome (Figure S2B). Notably, the mitochondrial genome of *B. distachyon* is not yet publicly available for footprint mapping.

The conservation of the light-dark response mechanism for subunit synthesis led us to investigate primitive plant cells. Here, we used Glaucophyta (*Cyanophora paradoxa*), which is considered the most ancient lineage in the kingdom Plantae (*48*, *49*). Chloroplasts of *C. paradoxa* resemble their cyanobacterial origin with the peptidoglycan "cell wall" between the membranes (*50*). Ribosome profiling of this species revealed the footprints of cytoribosomes and chlororibosomes (Figure S4A-G). We found that primordial chloroplasts already possessed a translational regulatory mechanism activated in response to light (Figures 3D and S4I-L). Thus, these data suggested the early implementation of translational control of chloroplastic gene expression during cyanobacterial symbiosis. Notably, in contrast to the RNA level control observed in the green lineages, cytoplasmic synthesis of subunits was regulated at the translational level

in Glaucophyta (Figures 3D and S4I-L), implying the divergence of regulatory strategies during evolution.

Switching of the regulatory mechanism upon endosymbiotic gene transfer

During coevolution, chloroplast-to-nuclear gene transfer (endosymbiotic gene transfer) shapes plant genomes. Although this gene transfer was largely completed at the early stage of symbiosis (*51*), independent events occurred in the green lineages. For example, *PsaI* in the PSI complex and *PetN* in Cyt b_6f were still encoded in the chloroplast genome in *Arabidopsis* but were transferred into the nuclear genome in *Chlamydomonas*. The mechanisms controlling light-dark transition-associated expression closely aligned with the gene locus (Figure 4A-B); specifically, the expression of chloroplast genome-encoded *PsaI* and *PetN* was regulated at the translational level in *Arabidopsis*, whereas the expression of these genes, encoded in the nuclear genome in *Chlamydomonas*, was altered at the RNA level in this species.

Moreover, the same gene transfer-coupled regulatory switch was found in paralogs within the same species. *Arabidopsis* possesses two paralogs of the PSII subunit *PsbT*, one encoded in the nuclear genome and the other in the chloroplast genome. Again, the responses of these *PsbT* paralogs to light/dark environments were driven by the general strategy predominant in each subcellular location: the paralog synthesized in the chloroplast stroma was under translational control, and the paralog synthesized in the cytoplasm was under RNA control (Figure 4C).

These data support the idea that the switch in the regulatory mechanism is associated with gene transfer from the chloroplast genome to the nuclear genome.

RNA level control is an ancestral mechanism in cyanobacteria

Considering the above findings, we sought to determine how cyanobacteria, the origin of chloroplasts, cope with changes in light conditions. Ribosome profiling and RNA-Seq analysis in *Synechocystis* sp. PCC6803 (Figure S5A-D) revealed that the F_oF_1 and NDH complexes (among others) exhibited on-demand dynamics in response to light cues (Figures 5A-B and S5H-J). However, this regulation relied mainly on changes in RNA abundances rather than on translational control (Figure 5A-B). Thus, these data suggested the conversion of the regulatory mechanism during chloroplast symbiosis from RNA-centric regulation in cyanobacteria to translation-centric regulation in chloroplasts (Figure 5C).

Reduced PQ increases translation in chloroplasts

Given the finding of light-dependent translational regulation in chloroplasts, we reasoned that photosynthesis may generate a signal to facilitate protein synthesis. To test this hypothesis, we treated *Arabidopsis* seedlings with 3-(3,4-dichlophenyl)1,1-dimethylurea (DCMU), a PSII inhibitor that blocks electron flux from PSII to PQ (*52*, *53*) (Figure 6A), in the dark and then exposed them to light (Figure 6B). The dark-to-light transition increased the translation efficiency of the chloroplastic mRNAs encoding complex subunits (Figure 6C), as observed in the previous experiments (Figures 2 and 3A). However, DCMU treatment attenuated this response (Figure 6C), indicating the pivotal role of the photosynthesis pathway in translational activation in chloroplasts.

Mechanistically, DCMU decreased the abundance of plastoquinol (PQH_2), the reduced form of PQ. Therefore, we evaluated the importance of PQH_2 for chloroplastic translation by treatment with 2,5-dibromo-3-methyl-6-isopropylbenzoquinone (DBMIB).

This compound inhibits electron flux to Cyt *b₆f* (*52–54*) (Figure 6A) and thus maintains the PQ pool in the form of PQH_2. Indeed, treatment of *Arabidopsis* seedlings with this compound under dark conditions (Figure 6D) induced effects mimicking those of light exposure, as we observed increases in the translation efficiency of complex subunits in chloroplasts (Figure 6E).

Coupling with photosynthesis and cytosolic mRNA abundances

On the other hand, our data suggest that PQH_2 itself is not involved in signaling controlling cytosolic mRNA abundances. DCMU decreased the efficiency of the induction of cytosolic mRNAs encoding chloroplastic complex subunits during the dark-to-light transition (Figures 6F and S6A). Thus, retrograde signaling—from the chloroplast to the cytoplasm/nucleus—plays a role in this response. On the other hand, DBMIB treatment under dark conditions did not increase the expression of these mRNAs (Figure S6B-C).

To investigate the evolutionary origin of this response, we repeated DCMU treatment in cyanobacteria, in which F_oF_1 and NDH complex synthesis is controlled at the RNA level (Figure 5A-B). DCMU attenuated the accumulation of the corresponding mRNAs in response to light (Figures 6G and S6D-E), suggesting that photosynthesis is a shared trigger for mRNA accumulation both in cyanobacteria and in the *Arabidopsis* cytosol.

Considering these data collectively, we concluded that chloroplasts use PQH_2 as a signaling molecule to balance the load of complex subunits used in the chloroplast stroma under light/dark conditions (Figure 6H).

Discussion

Orchestration of the subunit supply via dual gene expression systems is challenging. For this orchestration, in yeasts, cytosolic translation tunes mitochondrial translation (*13*). The present study highlights another mechanism underlying the balance in protein synthesis between dual genomes: control of RNA abundances in the cytosol and control of translation in chloroplasts. Light-dependent chloroplastic translation was initially reported in 3 decades ago (*55–57*) and has more recently been assessed at high resolution via chloroplast-tailored ribosome profiling (*29*, *58*). Our ribosome profiling for simultaneous assessment of translation via dual systems integrated the knowledge of chloroplastic translational regulation into a global view of the economy for multisubunit complexes.

Given the rapid decreases in cytosolic RNA abundances caused by light-to-dark shifts, mRNA decay is the most likely mechanism involved. This decay could be coordinated with transcriptional tuning, which may turn off mRNA synthesis under dark conditions and turn on under light conditions. In contrast to PQH_2-mediated mRNA splicing driven by exposure to light (*53*, *59*), the retrograde regulation of mRNA abundances reported in the present study may be driven by other signaling molecules, such as reactive oxygen species (ROS), isoprenoid precursors [methylerythritol cyclodiphosphate (MEcPP)], carotenoid derivatives, heme, and a phosphonucleotide [3′-phosphoadenosine 5′-phosphate (PAP)] (*60*). Since PAP was reported to function as an inhibitor of the 5′-to-3′ RNA exonuclease XRN2 in retrograde signaling (*61*), future investigations are warranted to determine its involvement.

In cyanobacteria, changes in mRNA abundances during light/dark transitions have previously been studied. Consistent with our observation, the occurrence of active

mRNA decay under dark conditions has been suggested (*62*). Conversely, light exposure inhibits mRNA decay (*62*) and simultaneously induces transcription through two-component regulatory systems involving histidine kinases and response regulators (*63*, *64*). Importantly, our ribosome profiling results showed that protein synthesis predominantly follows alterations in mRNA abundances, with no further need for translational regulation, at least for the short periods of darkness in our experiments. Longer exposure to dark conditions may trigger translational repression through the stringent response mediated by (p)ppGpp for adaptation (*65*).

Most likely, light-dependent chloroplastic translation is regulated at translation initiation, considering that this process is a global rate-limiting step in protein synthesis in growing cells (*66*–*72*) and generally determines ribosome footprint numbers on ORFs (*73*–*75*). This process may be mediated through mRNA-specific RNA-binding proteins and/or global translational regulators (through interactions with chlororibosomes) (*7*).

In addition to translation initiation, the elongation process can be subject to light-dependent regulation. *PsbA* (encoding D1, a catalytic center subunit of PSII) is a notable example of chlororibosome pausing (*76*, *77*). Our ribosome profiling results revealed stalling at this position (after exposure of the 4th transmembrane domain), consistent with earlier reports in *Arabidopsis* (*76*, *77*) (Figure S1B-C). Since this pausing on *PsbA* mRNA may exhibit interspecies variation (Figures S2H, S3H, S4H, and S5E-G), analysis of chloroplastic translation by disome profiling (*25*, *78*–*81*) will be useful.

Acknowledgments

We are grateful to all the members of the Iwasaki laboratory for fruitful discussion and technical help. We also thank Dr. Hiro-oki Iwakawa for the constructive advice. For this work, the supercomputer HOKUSAI Sailing Ship in RIKEN was used for computations. This study was supported by the Japan Society for the Promotion of Science (JSPS) (JP19H02959 and JP23H02415 to S.I.; JP19J14480 to T.F.; JP23KJ0444 to T.W.; JP23KJ2175 to N.K.; JP22K20765, JP23KJ2178, and JP23K14173 to H.T.; JP19K22434 and JP21H02509 to T.H.; JP23H05473 and JP23H04882 to M.Y.); the Ministry of Education, Culture, Sports, Science and Technology (MEXT) (JP20H05784 and JP24H02307 to S.I.); RIKEN (Pioneering Project "Biology of Intracellular Environments" to S.I. and M.M.; Incentive Research Project to H.T. and N.K.); and The University of Tokyo (C2205 and C2306 to T.W.). Some of the DNA libraries were sequenced by QB3 Genomics, UC Berkeley, Berkeley, CA (RRID: SCR_022170), which facilities were supported by an NIH Instrumentation Grant (S10 OD018174). T.F. was a recipient of the RIKEN Junior Research Associate Program and a JSPS Research Fellow (DC2). T.W. received fellowships from JSPS (DC2), JST SPRING (JPMJSP2108), and the ANRI. H.T. was a JSPS Research Fellow (PD). N.K. received the support of JSPS Research Fellow (PD) and the RIKEN Special Postdoctoral Researchers Program.

Author Contributions

Conceptualization: T.F. and S.I.;

Methodology: T.F., N.K., Y.K., Y.H., T.H., H.T., A.H., E.M.-S., and S.I.;

Formal analysis: T.F., T.W., N.K., H.T., and S.I.;

Investigation: T.F., T.W., N.K., Y.K., Y.H., T.H., H.T., T.K., A.H., and E.M.-S.;

Writing – Original Draft: N.K. and S.I.;

Writing – Review & Editing: T.F., T.W., N.K., Y.K., Y.H., T.H., H.T., T.K., A.H., E.M.-S., K.M., M.Y., M.M., and S.I.;

Visualization: T.F., T.W., N.K., and S.I.;

Supervision: Y.K., Y.H., T.H., K.M., M.Y., M.M., and S.I.;

Funding Acquisition: T.F., T.W., N.K., H.T., M.Y., M.M., and S.I.

Declaration of Interests

The authors declare no competing interests.

Materials and Methods

Culture of A. thaliana

Sterilized *A. thaliana* Col-0 seeds were sown on growth medium (1× Murashige and Skoog salt mixture, 10 g/l sucrose, and 0.8% agar; adjusted to pH 5.8), stored in the dark at 4°C for 3 d, and subsequently grown at 23°C under continuous exposure to white light (50 μmol/m^2/s) for 10 d. The plants were subsequently harvested before initiation of light/dark transitions (0 min); 30, 60, and 180 min after the light-to-dark transition; and 30, 60, and 90 min after the dark-to-light transition. The samples were flash-frozen in liquid nitrogen and stored at −80°C.

For compound treatment, 20 ml of the drug solution [10 mM MES (pH 5.8) with 10 μM DCMU, 30 μM DBMIB, or a corresponding amount of DMSO (solvent)] was poured onto the growth medium, and the drug-treated seedlings were subsequently grown in the dark at 23°C for 24 h. For the experiments with DCMU treatment, the plants were further incubated in the light for 180 min after the dark period.

Culture of B. distachyon

B. distachyon (Bd21) was grown on soil at 23°C on a 14-h light/10-h dark cycle for 25 d, followed by constant light conditions for 10 d. The plants were harvested before initiation of light/dark transitions (0 min); 30, 60, and 180 min after the light-to-dark transition; and 30, 60, and 90 min after the dark-to-light transition. The aboveground tissues from ten plants were pooled to generate one sample, flash-frozen in liquid nitrogen, and stored at −80°C.

Culture of C. reinhardtii

C. reinhardtii (NIES-2235) was obtained from the National Institute of Environmental Studies (NIES) culture collection. The cells were cultured in 50 ml of TAP medium in a 100-ml conical flask at 26°C with shaking at 100 rpm under constant exposure to white fluorescent light (MIR-254, PHCbi). The cells in a 30-ml volume of culture were collected on a 0.45-µm filter (Millipore) by vacuum filtration. The collected cells on the filter were immediately frozen in liquid nitrogen and stored at −80°C. Cultures were harvested before initiation of light/dark transitions(0 min); 15 and 90 min after the light-to-dark transition; and 15 and 90 min after the dark-to-light transition.

Culture of C. paradoxica

C. paradoxa (NIES-547) was obtained from the NIES culture collection. The cells were aseptically cultured in 6 square glass flasks that contained 800 ml of Bold 3N liquid medium for 14 d at 26°C under constant exposure to white fluorescent light (10 µE/m^2/s) with 1% CO_2 (v/v) bubbling (*82*). The cells in a 200-ml volume of culture were collected on two 0.45-µm filters (Millipore) by vacuum filtration. The collected cells on the filters were immediately frozen in liquid nitrogen and stored at −80°C. Cultures were harvested before initiation of light/dark transitions (0 min); 15 and 90 min after the light-to-dark transition; and 15 and 90 min after the dark-to-light transition.

Culture of Synechocystis sp. PCC6803

Synechocystis sp. PCC6803 was cultivated in BG-11 liquid medium (*83*) at 30°C under continuous exposure to white light (50 µmol/m^2/s) with shaking (160 rpm). The cells in a 30-ml volume of culture were collected on a 0.45-µm filter (Millipore) by vacuum filtration. The collected cells on the filter were immediately frozen in liquid nitrogen and

stored at −80°C. Cultures were harvested before initiation of light/dark transitions (0 min); 15 and 90 min after the light-to-dark transition; and 15 and 90 min after the dark-to-light transition.

For compound treatment, cells were cultured in 30 ml of medium containing 10 μM DCMU, 10 μM DBMIB, or a corresponding amount of DMSO (solvent). The drug-treated cells were incubated in the dark at 30°C for 24 h. For the experiments with DCMU treatment, the cells were further incubated in the light for 90 min after the dark period.

Lysate preparation for ribosome profiling and RNA-Seq analysis

For *A. thaliana* and *B. distachyon*, frozen samples were pulverized with 400 μl of frozen lysis buffer [100 mM Tris-HCl (pH 7.5), 40 mM KCl, 20 mM $MgCl_2$, 1 mM dithiothreitol (DTT), 1% Triton X-100, 300 μg/ml chloramphenicol, and 100 μg/ml cycloheximide] using a Multi-beads Shocker instrument (Yasui Kikai) at 2800 rpm for 10 s.

For *C. reinhardtii*, pulverization was performed by 2 cycles at 1500 rpm for 15 s with 650 μl of frozen lysis buffer. The lysate was thawed on ice and immediately clarified by centrifugation at 3,000 × g for 5 min at 4°C. The supernatant was incubated with 25 U/ml Turbo DNase (Thermo Fisher Scientific) and clarified by centrifugation at 20,000 × g for 10 min at 4°C.

For *C. paradoxa*, pulverization was performed with 650 μl of frozen lysis buffer at 2800 rpm for 10 s. The lysate was thawed on ice and filtered through Spin-X Centrifuge Tube Filters (0.22 μm Pore CA Membrane, Costor) by centrifugation at 16,000 × g for 5 min at 4°C. Then, the flowthrough was incubated with 25 U/ml Turbo DNase (Thermo Fisher Scientific) and clarified by centrifugation at 20,000 × g for 10 min at 4°C.

For *Synechocystis* sp. PCC6803, pulverization was performed by 2 cycles of 1500 rpm for 15 s with 400 µl of frozen bacterial lysis buffer [20 mM Tris-HCl (pH 7.5), 150 mM NH_4Cl, 10 mM $MgCl_2$, 5 mM $CaCl_2$, 1 mM DTT, 1% Triton X-100, and 100 µg/ml chloramphenicol]. The lysate was thawed on ice and immediately clarified by centrifugation at 3,000 × g for 5 min at 4°C. The supernatant was incubated with 25 U/ml Turbo DNase (Thermo Fisher Scientific) on ice and clarified by centrifugation at 20,000 × g for 10 min at 4°C.

Library preparation for ribosome profiling

Library preparation for ribosome profiling was performed as previously described (*22*, *84*, *85*). The RNA content in each lysate was measured with a Qubit RNA BR Assay Kit (Thermo Fisher Scientific). The lysates were treated with 20 U of RNase I (LGC Biosearch Technologies) for *A. thaliana* (30 µg of RNA), *B. distachyon* (30 µg of RNA), and *C. paradoxa* (30 µg of RNA); with 10 U of RNase I for *C. reinhardtii* (20 µg of RNA); or with 15 U of MNase (Roche) for *Synechocystis* sp. PCC6803 (20 µg of RNA). All of the above enzymatic treatments were performed in a 300-µl reaction (scaled up by the amount of lysis buffer or bacterial lysis buffer) at 25°C for 45 min. After the ribosomes were collected on a sucrose cushion, RNA was extracted with TRIzol (Thermo Fisher Scientific) and a Direct-zol RNA MicroPrep Kit (Zymo Research). After separation on a 15% urea polyacrylamide gel electrophoresis (PAGE) gel, RNA fragments containing 17 to 50 nt were excised from the gel, dephosphorylated, and ligated with linkers. rRNAs were depleted with the following kits: a Ribo-Zero Gold rRNA Removal Kit (Plant Leaf) (Illumina) for *A. thaliana, C. reinhardtii*, and *B. distachyon*; a RiboMinus Plant Kit for RNA-Seq (Thermo Fisher Scientific) for *C. paradoxa*; and a

Ribo-Zero Gold rRNA Removal Kit (Bacteria) (Illumina) or Pan-Bacteria riboPOOLs (siTOOLs Biotech) for *Synechocystis* sp. PCC6803. cDNAs were synthesized by reverse transcription, subjected to circular ligation, and amplified by PCR. The DNA libraries were sequenced on the HiSeq 4000, HiSeq X, or NovaSeq 6000 platform. The libraries used for this study are summarized in Table S1.

Library preparation for RNA-Seq

Total RNA was extracted from the same lysates used for ribosome profiling with TRIzol LS (Thermo Fisher Scientific) and a Direct-zol RNA MicroPrep Kit (Zymo Research). After rRNA depletion (see the "*Library preparation for ribosome profiling*" section), the libraries were prepared with a TruSeq Stranded mRNA Library Prep Kit (Illumina) and sequenced on the HiSeq 4000 or HiSeq X platform. The libraries used for this study are summarized in Table S1.

Data analysis

The deep sequencing data were processed as reported previously with modifications (*86*). Read quality filtering and adapter trimming were performed with fastp (version 0.21.0) (*87*). After all reads aligned to noncoding RNAs were removed using STAR (version 2.7.0a) (*88*), the unaligned reads were mapped to the corresponding nuclear, mitochondrial, and chloroplastic genomes [*A. thaliana*, TAIR10; *B. distachyon*, GCA_000005505.4 (nuclear genome) and NC_011032.1 (chloroplast genome); *C. reinhardtii*, GCA_000002595.3 (nuclear genome), U03843.1 (mitochondrial genome), and NC_005353.1 (chloroplast genome); *C. paradoxa*, ASM443141v1 (nuclear genome), NC_017836.1 (mitochondrial genome), and NC_001675.1 (chloroplast genome); and

Synechocystis sp. PCC6803, ASM972v1] using STAR. For *Escherichia coli*, reads were first aligned to noncoding RNAs using Bowtie2 (version 2.4.1) (*89*), and these aligned reads were excluded from the downstream analysis. The remaining reads were mapped to the *E. coli* genome sequence (NC_000913.2) with Bowtie2. For ribosome profiling, the A-site position offsets from the 5′ ends of the reads were empirically determined for each read length, as summarized in Table S1. For RNA-Seq analysis, an offset of 15 was applied.

Reads assigned to ORFs were counted with a custom script (https://github.com/ingolia-lab/RiboSeq), and reads whose A sites were located in the first and last 5 codons were excluded. The relative enrichment of ribosome profiling and RNA-Seq reads was calculated with the DESeq2 package (*90*). Translation efficiency was calculated via a generalized linear model with the DESeq2 package.

Data availability

The ribosome profiling and RNA-Seq data obtained in this study were deposited in the National Center for Biotechnology Information (NCBI) database. We also used bacterial ribosome profiling data published in an earlier work (GSE180482) (*85*).

Code availability

For ribosome profiling and RNA-Seq data analysis, we used the deposited codes [Zenodo 5675739 (https://doi.org/10.5281/zenodo.5675739)] (*86*) and amended them accordingly.

Figure and table legends

Figure 1. Simultaneous assessment of cytosolic and chloroplastic translations by ribosome profiling.

(A) Schematic representation of the procedure for plant ribosome profiling, which recovers footprints stemming from cytoribosomes and chlororibosomes.

(B) Pie chart showing the proportions of footprints from cytoribosomes, mitoribosomes, and chlororibosomes in *A. thaliana*.

(C) Length distribution of cytoribosome footprints and chlororibosome footprints.

(D and E) Metagene plots of the 5′ ends of cytoribosome footprints (D) and chlororibosome footprints (E) along the length around start codons (the first nucleotide of the start codon was set to 0). The color scale indicates the read abundance. RPM, reads per million mapped reads.

(F and G) Discrete Fourier transform of cytoribosome footprints (28 nt) (F) and chlororibosome footprints (24 nt) (G) downstream of the start codon (from position -9 to position 300).

(H) Correlation between the normalized read density (reads/codon) and the subunit stoichiometry for the chloroplast F_oF_1 ATP synthase.

See also Figure S1 and Table S1.

Figure 2. Light/dark transitions coordinate the protein supply via dual gene expression systems.

(A) Schematic representation of the experimental design used to monitor the light-dependent synthesis of the subunits of thylakoid membrane-embedded complexes.

(B-F) Changes in ribosome profiling, RNA-Seq, and translation efficiency during the light-to-dark and dark-to-light transitions for the subunits of F_oF_1 ATP synthase (B), PSII (C), Cyt b_6f (D), PSI (E), and NDH (F) in *A. thaliana*. The box plots show the median (center line), upper/lower quartiles (box limits), and 1.5× interquartile range (whiskers). The black line indicates the median at each time point.

See also Table S1.

Figure 3. Conservation of the regulation of cytosolic mRNA abundances and chloroplastic translation.

(A-D) Changes in ribosome profiling, RNA-Seq, and translation efficiency during the light-to-dark and dark-to-light transitions for the subunits of F_oF_1 ATP synthase, PSII, Cyt b_6f, PSI, and NDH in *A. thaliana* (A), *B. distachyon* (B), *C. reinhardtii* (C), and *C. paradoxa* (D). *C. reinhardtii* and *C. paradoxa* do not possess NDH. The box plots show the median (center line), upper/lower quartiles (box limits), and 1.5× interquartile range (whiskers). The black line indicates the median at each time point.

See also Figures S2-4 and Table S1.

Figure 4. Switch in the regulatory mechanism associated with endosymbiotic gene transfer.

(A-B) Changes in ribosome profiling, RNA-Seq, and translation efficiency during the light-to-dark and dark-to-light transitions for *PsaI* (A, a subunit of the PSI complex) and *PetN* (B, a subunit of Cyt b_6f) in *A. thaliana* and *C. reinhardtii*.

(C) Changes in ribosome profiling, RNA-Seq, and translation efficiency during the light-to-dark and dark-to-light transitions for paralogs of *PsbT* (a subunit of PSII) in *A. thaliana*.

Figure 5. Absence of light-dependent translational regulation in cyanobacteria.

(A-B) Changes in ribosome profiling, RNA-Seq, and translation efficiency during the light-to-dark and dark-to-light transitions for the subunits of F_oF_1 ATP synthase (A) and NDH (B) in *Synechocystis* sp. PCC6803. The box plots show the median (center line), upper/lower quartiles (box limits), and 1.5× interquartile range (whiskers). The black line indicates the median at each time point.

(C) Model of light-dependent regulation of the assembly of the photosynthetic apparatus among species.

See also Figure S5 and Table S1.

Figure 6. PQH_2 triggers translational activation in chloroplasts.

(A) Schematic representation of the inhibitory mechanisms of DCMU and DBMIB.

(B) Schematic representation of the experimental design used to monitor the response of cytosolic and chloroplastic gene expression to DCMU treatment.

(C) Fold change in the translation efficiency following DCMU treatment of *A. thaliana* during the dark-to-light transition. Cytosolic mRNAs and chloroplast mRNAs encoding the subunits of F_oF_1 ATP synthase, PSII, Cyt b_6f, PSI, and NDH were analyzed. The box plots show the median (center line), upper/lower quartiles (box limits), and 1.5× interquartile range (whiskers). Significance was determined by the Mann–Whitney *U* test.

(D) Schematic representation of the experimental design used to monitor the response of cytosolic and chloroplastic gene expression to DBMIB treatment.

(E) Cumulative distribution of the fold changes in the translation efficiency caused by DBMIB treatment in *A. thaliana* under dark conditions. mRNAs encoding the subunits

of F_oF_1 ATP synthase, PSII, Cyt *b₆f*, PSI, and NDH were compared to the total mRNAs. Significance was determined by the Mann–Whitney *U* test.

(F) Fold changes in RNA abundances following DCMU treatment of *A. thaliana* during the dark-to-light transition. Cytosolic mRNAs and chloroplast mRNAs encoding the subunits of F_oF_1 ATP synthase, PSII, Cyt *b₆f*, PSI, and NDH were analyzed. The box plots show the median (center line), upper/lower quartiles (box limits), and 1.5× interquartile range (whiskers). Significance was determined by the Mann–Whitney *U* test.

(G) Fold changes in RNA abundances following DCMU treatment of *Synechocystis* sp. PCC6803 during the dark-to-light transition. mRNAs encoding the subunits of F_oF_1 ATP synthase (left) and NDH (right) were analyzed. The box plots show the median (center line), upper/lower quartiles (box limits), and 1.5× interquartile range (whiskers). Significance was determined by the Mann–Whitney *U* test.

(H) Model of the distinct mechanisms employed for cytoplasmic and chloroplastic gene expression in response to light exposure.

See also Figure S6 and Table S1.

Figure S1. Characterization of ribosome profiling data in *A. thaliana*, related to Figure 1.

(A) Metagene plots of the 5′ ends of bacterial ribosome footprints along the length around start codons (the first nucleotide of the start codon was set to 0). The color scale indicates the read abundance.

(B) Distributions of chlororibosome footprints along the *PsbA* mRNA under the indicated conditions. The A-site position of each read (the start codon was set to 0) is indicated.

(C) Schematic representation of configurations of chlororibosome pause sites found in *PsbA* with cotranslational insertion of the nascent peptide into the thylakoid membrane.

Figure S2. Characterization of ribosome profiling data in *B. distachyon*, related to Figure 3.

(A) Pie chart showing the proportions of footprints from cytoribosomes and chlororibosomes in *B. distachyon*. Mitoribosome footprints were not assigned due to a lack of the mitochondrial genome sequence.

(B) Length distributions of cytoribosome footprints and chlororibosome footprints.

(C and D) Metagene plots of the 5′ ends of cytoribosome footprints (C) and chlororibosome footprints (D) along the length around start codons (the first nucleotide of the start codon was set to 0). The color scale indicates the read abundance. RPM, reads per million mapped reads.

(E and F) Discrete Fourier transform of cytoribosome footprints (28 nt) (E) and chlororibosome footprints (25 nt) (F) downstream of the start codon (from position -9 to position 300).

(G) Correlation between the normalized read density (reads/codon) and the subunit stoichiometry for the chloroplast F_oF_1 ATP synthase.

(H) Distributions of chlororibosome footprints along the *PsbA* mRNA under the indicated conditions. The A-site position of each read (the start codon was set to 0) is indicated.

(I-M) Changes in ribosome profiling, RNA-Seq, and translation efficiency during the light-to-dark and dark-to-light transitions for the subunits of F_oF_1 ATP synthase (I), PSII (J), Cyt b_6f (K), PSI (L), and NDH (M) in *B. distachyon*. The box plots show the median

(center line), upper/lower quartiles (box limits), and 1.5× interquartile range (whiskers). The black line indicates the median at each time point.

(N) Changes in ribosome profiling, RNA-Seq, and translation efficiency during the light-to-dark and dark-to-light transitions for the subunits of F_oF_1 ATP synthase, PSII, Cyt b_6f, PSI, and NDH among the nuclear plastid genes in *B. distachyon*. The box plots show the median (center line), upper/lower quartiles (box limits), and 1.5× interquartile range (whiskers). The black line indicates the median at each time point.

Figure S3. Characterization of ribosome profiling data in *C. reinhardtii*, related to Figure 3.

(A) Pie chart showing the proportions of footprints from cytoribosomes and chlororibosomes in *C. reinhardtii*.

(B) Length distributions of cytoribosome footprints and chlororibosome footprints.

(C and D) Metagene plots of the 5′ ends of cytoribosome footprints (C) and chlororibosome footprints (D) along the length around start codons (the first nucleotide of the start codon was set to 0). The color scale indicates the read abundance. RPM, reads per million mapped reads.

(E and F) Discrete Fourier transform of cytoribosome footprints (31 nt) (E) and chlororibosome footprints (27 nt) (F) downstream of the start codon (from position -9 to position 300).

(G) Correlation between the normalized read density (reads/codon) and the subunit stoichiometry for the chloroplast F_oF_1 ATP synthase.

(H) Distributions of chlororibosome footprints along the *PsbA* mRNA under the indicated conditions. The A-site position of each read (the start codon was set to 0) is indicated.

(I-L) Changes in ribosome profiling, RNA-Seq, and translation efficiency during the light-to-dark and dark-to-light transitions for the subunits of F_oF_1 ATP synthase (I), PSII (J), Cyt b_6f (K), and PSI (L) in *C. reinhardtii*. The box plots show the median (center line), upper/lower quartiles (box limits), and 1.5× interquartile range (whiskers). The black line indicates the median at each time point.

Figure S4. Characterization of ribosome profiling data for *C. paradoxa*, related to Figure 3.

(A) Pie chart showing the proportions of footprints from cytoribosomes and chlororibosomes in *C. paradoxa*.

(B) Length distributions of cytoribosome footprints and chlororibosome footprints.

(C and D) Metagene plots of the 5′ ends of cytoribosome footprints (C) and chlororibosome footprints (D) along the length around start codons (the first nucleotide of the start codon was set to 0). The color scale indicates the read abundance. RPM, reads per million mapped reads.

(E and F) Discrete Fourier transform of cytoribosome footprints (30 nt) (E) and chlororibosome footprints (33 nt) (F) downstream of the start codon (from position -9 to position 300).

(G) Correlation between the normalized read density (reads/codon) and the subunit stoichiometry for the chloroplast F_oF_1 ATP synthase.

(H) Distributions of chlororibosome footprints along the *PsbA* mRNA under the indicated conditions. The A-site position of each read (the start codon was set to 0) is indicated.

(I-L) Changes in ribosome profiling, RNA-Seq, and translation efficiency during the light-to-dark and dark-to-light transitions for the subunits of F_oF_1 ATP synthase (I), PSII

(J), Cyt b_6f (K), and PSI (L) in *C. paradoxa*. The box plots show the median (center line), upper/lower quartiles (box limits), and 1.5× interquartile range (whiskers). The black line indicates the median at each time point.

Figure S5. Characterization of ribosome profiling data in *Synechocystis* sp. PCC6803, related to Figure 5.

(A) Length distributions of ribosome footprints and chlororibosome footprints in *Synechocystis* sp. PCC6803.

(B) Metagene plots of the 5′ ends of ribosome footprints along the length around start codons (the first nucleotide of the start codon was set to 0). The color scale indicates the read abundance. RPM, reads per million mapped reads.

(C) Discrete Fourier transform of ribosome footprints (27 nt) downstream of the start codon (from position -9 to position 300).

(D) Correlation between the normalized read density (reads/codon) and the subunit stoichiometry for the chloroplast F_oF_1 ATP synthase.

(E-G) Distributions of chlororibosome footprints along the *PsbA1* (E), *PsbA2* (F), and *PsbA3* (G) mRNAs under the indicated conditions. The A-site position of each read (the start codon was set to 0) is indicated.

(H-J) Changes in ribosome profiling, RNA-Seq, and translation efficiency during the light-to-dark and dark-to-light transitions for the subunits of PSII (H), Cyt b_6f (I), and PSI (J) in *Synechocystis* sp. PCC6803. The box plots show the median (center line), upper/lower quartiles (box limits), and 1.5× interquartile range (whiskers). The black line indicates the median at each time point.

Figure S6. Characterization of DCMU and DBMIB treatment, related to Figure 6.

(A) Fold changes in the ribosome footprint following DCMU treatment of *A. thaliana* during the dark-to-light transition. Cytosolic mRNAs and chloroplast mRNAs encoding the subunits of F_oF_1 ATP synthase, PSII, Cyt b_6f, PSI, and NDH were analyzed. The box plots show the median (center line), upper/lower quartiles (box limits), and 1.5× interquartile range (whiskers). Significance was determined by the Mann–Whitney *U* test.

(B-C) Cumulative distributions of fold changes in ribosome footprints (B) and RNA abundances (C) following DBMIB treatment of *A. thaliana* in the dark. mRNAs encoding the subunits of F_oF_1 ATP synthase, PSII, Cyt b_6f, PSI, and NDH were compared to the total mRNAs. Significance was determined by the Mann–Whitney *U* test.

(D) Fold changes in ribosome footprints following DCMU treatment of *Synechocystis* sp. PCC6803 during the dark-to-light transition. mRNAs encoding the subunits of F_oF_1 ATP synthase (left) and NDH (right) were analyzed. The box plots show the median (center line), upper/lower quartiles (box limits), and 1.5× interquartile range (whiskers). Significance was determined by the Mann–Whitney *U* test.

(G) Fold change in the translation efficiency following DCMU treatment of *Synechocystis* sp. PCC6803 during the dark-to-light transition. mRNAs encoding the subunits of F_oF_1 ATP synthase (left) and NDH (right) were analyzed. The box plots show the median (center line), upper/lower quartiles (box limits), and 1.5× interquartile range (whiskers). Significance was determined by the Mann–Whitney *U* test.

Table S1. List of ribosome profiling and RNA-Seq libraries, related to Figures 1-3 and 5-6.

For each data set, the library name, species, strain name, light/dark conditions, drug treatment, replicate number, library type, the read length used for cytoribosome footprints, A-site offsets for cytoribosome footprints, the read length used for chlororibosome footprints, A-site offsets for chlororibosome footprints, the read length used for mitoribosome footprints, A-site offsets for mitoribosome footprints, accession numbers, and references are listed.

References

1. N. Nelson, A. Ben-Shem, The complex architecture of oxygenic photosynthesis. *Nat. Rev. Mol. Cell Biol.* **5**, 971–982 (2004).

2. G. Peltier, E.-M. Aro, T. Shikanai, NDH-1 and NDH-2 plastoquinone reductases in oxygenic photosynthesis. *Annu. Rev. Plant Biol.* **67**, 55–80 (2016).

3. A. Hahn, J. Vonck, D. J. Mills, T. Meier, W. Kühlbrandt, Structure, mechanism, and regulation of the chloroplast ATP synthase. *Science* **360** (2018).

4. T. Bai, L. Guo, M. Xu, L. Tian, Structural diversity of photosystem I and its light-harvesting system in eukaryotic algae and plants. *Front. Plant Sci.* **12**, 781035 (2021).

5. D. Shevela, J. F. Kern, G. Govindjee, J. Messinger, Solar energy conversion by photosystem II: principles and structures. *Photosynth. Res.* **156**, 279–307 (2023).

6. J. F. Allen, W. B. M. de Paula, S. Puthiyaveetil, J. Nield, A structural phylogenetic map for chloroplast photosynthesis. *Trends Plant Sci.* **16**, 645–655 (2011).

7. R. Zoschke, R. Bock, Chloroplast translation: structural and functional organization, operational control, and regulation. *Plant Cell* **30**, 745–770 (2018).

8. S. Juszkiewicz, R. S. Hegde, Quality control of orphaned proteins. *Mol. Cell* **71**, 443–457 (2018).

9. J. C. Taggart, H. Zauber, M. Selbach, G.-W. Li, E. McShane, Keeping the proportions of protein complex components in check. *Cell Syst* **10**, 125–132

(2020).

10. S. F. Pearce, P. Rebelo-Guiomar, A. R. D'Souza, C. A. Powell, L. Van Haute, M. Minczuk, Regulation of mammalian mitochondrial gene expression: recent advances. *Trends Biochem. Sci.* **42**, 625–639 (2017).

11. D. B. Sloan, J. M. Warren, A. M. Williams, Z. Wu, S. E. Abdel-Ghany, A. J. Chicco, J. C. Havird, Cytonuclear integration and co-evolution. *Nat. Rev. Genet.* **19**, 635–648 (2018).

12. E. Kummer, N. Ban, Mechanisms and regulation of protein synthesis in mitochondria. *Nat. Rev. Mol. Cell Biol.* **22**, 307–325 (2021).

13. M. T. Couvillion, I. C. Soto, G. Shipkovenska, L. S. Churchman, Synchronized mitochondrial and cytosolic translation programs. *Nature* **533**, 499–503 (2016).

14. N. T. Ingolia, S. Ghaemmaghami, J. R. Newman, J. S. Weissman, Genome-wide analysis *in vivo* of translation with nucleotide resolution using ribosome profiling. *Science* **324**, 218–223 (2009).

15. T. Fujita, Y. Kurihara, S. Iwasaki, The plant translatome surveyed by ribosome profiling. *Plant Cell Physiol.* **60**, 1917–1926 (2019).

16. S. Iwasaki, S. N. Floor, N. T. Ingolia, Rocaglates convert DEAD-box protein eIF4A into a sequence-selective translational repressor. *Nature* **534**, 558–561 (2016).

17. T. Y. Liu, H. H. Huang, D. Wheeler, Y. Xu, J. A. Wells, Y. S. Song, A. P. Wiita, Time-resolved proteomics extends ribosome profiling-based measurements of

protein synthesis dynamics. *Cell Syst* **4**, 636–644.e9 (2017).

18. Q. Li, H. Yang, E. K. Stroup, H. Wang, Z. Ji, Low-input RNase footprinting for simultaneous quantification of cytosolic and mitochondrial translation. *Genome Res.* **32**, 545–557 (2022).

19. L. F. Lareau, D. H. Hite, G. J. Hogan, P. O. Brown, Distinct stages of the translation elongation cycle revealed by sequencing ribosome-protected mRNA fragments. *Elife* **3**, e01257 (2014).

20. F. Mohammad, C. J. Woolstenhulme, R. Green, A. R. Buskirk, Clarifying the translational pausing landscape in bacteria by ribosome profiling. *Cell Rep.* **14**, 686–694 (2016).

21. N. R. Guydosh, R. Green, Translation of poly(A) tails leads to precise mRNA cleavage. *RNA* **23**, 749–761 (2017).

22. Y. Kurihara, Y. Makita, M. Kawashima, T. Fujita, S. Iwasaki, M. Matsui, Transcripts from downstream alternative transcription start sites evade uORF-mediated inhibition of gene expression in Arabidopsis. *Proc. Natl. Acad. Sci. U. S. A.* **115**, 7831–7836 (2018).

23. C. C. Wu, B. Zinshteyn, K. A. Wehner, R. Green, High-resolution ribosome profiling defines discrete ribosome elongation states and translational regulation during cellular stress. *Mol. Cell* **73**, 959–970.e5 (2019).

24. F. Mohammad, R. Green, A. R. Buskirk, A systematically-revised ribosome profiling method for bacteria reveals pauses at single-codon resolution. *Elife* **8**,

e42591 (2019).

25. P. Han, Y. Shichino, T. Schneider-Poetsch, M. Mito, S. Hashimoto, T. Udagawa, K. Kohno, M. Yoshida, Y. Mishima, T. Inada, S. Iwasaki, Genome-wide survey of ribosome collision. *Cell Rep.* **31**, 107610 (2020).

26. B. Y. Chung, T. J. Hardcastle, J. D. Jones, N. Irigoyen, A. E. Firth, D. C. Baulcombe, I. Brierley, The use of duplex-specific nuclease in ribosome profiling and a user-friendly software package for Ribo-seq data analysis. *RNA* **21**, 1731–1745 (2015).

27. P. Chotewutmontri, A. Barkan, Dynamics of chloroplast translation during chloroplast differentiation in maize. *PLoS Genet.* **12**, e1006106 (2016).

28. R. Zoschke, P. Chotewutmontri, A. Barkan, Translation and co-translational membrane engagement of plastid-encoded chlorophyll-binding proteins are not influenced by chlorophyll availability in maize. *Front. Plant Sci.* **8**, 385 (2017).

29. P. Chotewutmontri, A. Barkan, Multilevel effects of light on ribosome dynamics in chloroplasts program genome-wide and psbA-specific changes in translation. *PLoS Genet.* **14**, e1007555 (2018).

30. P. Gawroński, P. E. Jensen, S. Karpiński, D. Leister, L. B. Scharff, Pausing of chloroplast ribosomes is induced by multiple features and is linked to the assembly of photosynthetic complexes. *Plant Physiol.* **176**, 2557–2569 (2018).

31. J. Shine, L. Dalgarno, The 3'-terminal sequence of *Escherichia coli* 16S ribosomal RNA: complementarity to nonsense triplets and ribosome binding sites. *Proc. Natl.*

Acad. Sci. U. S. A. **71**, 1342–1346 (1974).

32. T. Kaminishi, D. N. Wilson, C. Takemoto, J. M. Harms, M. Kawazoe, F. Schluenzen, K. Hanawa-Suetsugu, M. Shirouzu, P. Fucini, S. Yokoyama, A snapshot of the 30S ribosomal subunit capturing mRNA via the Shine-Dalgarno interaction. *Structure* **15**, 289–297 (2007).

33. J. Kim, J. E. Mullet, Ribosome-binding sites on chloroplast *rbcL* and *psbA* mRNAs and light-induced initiation of D1 translation. *Plant Mol. Biol.* **25**, 437–448 (1994).

34. D. C. Fargo, M. Zhang, N. W. Gillham, J. E. Boynton, Shine-Dalgarno-like sequences are not required for translation of chloroplast mRNAs in *Chlamydomonas reinhardtii* chloroplasts or in *Escherichia coli*. *Mol. Gen. Genet.* **257**, 271–282 (1998).

35. T. Hirose, M. Sugiura, Functional Shine-Dalgarno-like sequences for translational initiation of chloroplast mRNAs. *Plant Cell Physiol.* **45**, 114–117 (2004).

36. O. Drechsel, R. Bock, Selection of Shine-Dalgarno sequences in plastids. *Nucleic Acids Res.* **39**, 1427–1438 (2011).

37. L. B. Scharff, L. Childs, D. Walther, R. Bock, Local absence of secondary structure permits translation of mRNAs that lack ribosome-binding sites. *PLoS Genet.* **7**, e1002155 (2011).

38. M. Sugiura, Plastid mRNA translation. *Methods Mol. Biol.* **1132**, 73–91 (2014).

39. L. B. Scharff, M. Ehrnthaler, M. Janowski, L. H. Childs, C. Hasse, J. Gremmels, S. Ruf, R. Zoschke, R. Bock, Shine-Dalgarno sequences play an essential role in the

translation of plastid mRNAs in tobacco. *Plant Cell* **29**, 3085–3101 (2017).

40. Y. Wei, X. Xia, Unique Shine-Dalgarno sequences in cyanobacteria and chloroplasts reveal evolutionary differences in their translation initiation. *Genome Biol. Evol.* **11**, 3194–3206 (2019).

41. G. W. Li, D. Burkhardt, C. Gross, J. S. Weissman, Quantifying absolute protein synthesis rates reveals principles underlying allocation of cellular resources. *Cell* **157**, 624–635 (2014).

42. J.-B. Lalanne, J. C. Taggart, M. S. Guo, L. Herzel, A. Schieler, G.-W. Li, Evolutionary convergence of pathway-specific enzyme expression stoichiometry. *Cell* **173**, 749–761.e38 (2018).

43. J. C. Taggart, G.-W. Li, Production of protein-complex components is stoichiometric and lacks general feedback regulation in eukaryotes. *Cell Syst* **7**, 580–589.e4 (2018).

44. R. Lukoszek, P. Feist, Z. Ignatova, Insights into the adaptive response of *Arabidopsis thaliana* to prolonged thermal stress by ribosomal profiling and RNA-Seq. *BMC Plant Biol.* **16**, 221 (2016).

45. R. Trösch, R. Barahimipour, Y. Gao, J. A. Badillo-Corona, V. L. Gotsmann, D. Zimmer, T. Mühlhaus, R. Zoschke, F. Willmund, Commonalities and differences of chloroplast translation in a green alga and land plants. *Nat Plants* **4**, 564–575 (2018).

46. R. Hasterok, P. Catalan, S. P. Hazen, A. C. Roulin, J. P. Vogel, K. Wang, L. A. J.

Mur, Brachypodium: 20 years as a grass biology model system; the way forward? *Trends Plant Sci.* **27**, 1002–1016 (2022).

47. Y. Chen, Y. Guo, X. Xie, Z. Wang, L. Miao, Z. Yang, Y. Jiao, C. Xie, J. Liu, Z. Hu, M. Xin, Y. Yao, Z. Ni, Q. Sun, H. Peng, W. Guo, Pangenome-based trajectories of intracellular gene transfers in Poaceae unveil high cumulation in Triticeae. *Plant Physiol.* **193**, 578–594 (2023).

48. D. C. Price, C. X. Chan, H. S. Yoon, E. C. Yang, H. Qiu, A. P. M. Weber, R. Schwacke, J. Gross, N. A. Blouin, C. Lane, A. Reyes-Prieto, D. G. Durnford, J. A. D. Neilson, B. F. Lang, G. Burger, J. M. Steiner, W. Löffelhardt, J. E. Meuser, M. C. Posewitz, S. Ball, M. C. Arias, B. Henrissat, P. M. Coutinho, S. A. Rensing, A. Symeonidi, H. Doddapaneni, B. R. Green, V. D. Rajah, J. Boore, D. Bhattacharya, *Cyanophora paradoxa* genome elucidates origin of photosynthesis in algae and plants. *Science* **335**, 843–847 (2012).

49. F. W. Spiegel, Evolution. Contemplating the first Plantae, *Science*. **335** (2012)pp. 809–810.

50. B. Pfanzagl, A. Zenker, E. Pittenauer, G. Allmaier, J. Martinez-Torrecuadrada, E. R. Schmid, M. A. De Pedro, W. Löffelhardt, Primary structure of cyanelle peptidoglycan of Cyanophora paradoxa: a prokaryotic cell wall as part of an organelle envelope. *J. Bacteriol.* **178**, 332–339 (1996).

51. E. Filip, L. Skuza, Horizontal Gene Transfer Involving Chloroplasts. *Int. J. Mol. Sci.* **22** (2021).

52. A. Khandelwal, T. Elvitigala, B. Ghosh, R. S. Quatrano, *Arabidopsis* transcriptome reveals control circuits regulating redox homeostasis and the role of an AP2 transcription factor. *Plant Physiol.* **148**, 2050–2058 (2008).

53. E. Petrillo, M. A. Godoy Herz, A. Fuchs, D. Reifer, J. Fuller, M. J. Yanovsky, C. Simpson, J. W. S. Brown, A. Barta, M. Kalyna, A. R. Kornblihtt, A chloroplast retrograde signal regulates nuclear alternative splicing. *Science* **344**, 427–430 (2014).

54. G. Schansker, S. Z. Tóth, R. J. Strasser, Methylviologen and dibromothymoquinone treatments of pea leaves reveal the role of photosystem I in the Chl a fluorescence rise OJIP. *Biochim. Biophys. Acta* **1706**, 250–261 (2005).

55. M. Taniguchi, H. Kuroda, K. Satoh, ATP-dependent protein synthesis in isolated pea chloroplasts. Evidence for accumulation of a translation intermediate of the D1 protein. *FEBS Lett.* **317**, 57–61 (1993).

56. S. K. Mühlbauer, L. A. Eichacker, Light-dependent formation of the photosynthetic proton gradient regulates translation elongation in chloroplasts. *J. Biol. Chem.* **273**, 20935–20940 (1998).

57. L. Zhang, V. Paakkarinen, K. J. van Wijk, E. M. Aro, Co-translational assembly of the D1 protein into photosystem II. *J. Biol. Chem.* **274**, 16062–16067 (1999).

58. P. Gawroński, C. Enroth, P. Kindgren, S. Marquardt, S. Karpiński, D. Leister, P. E. Jensen, J. Vinther, L. B. Scharff, Light-dependent translation change of Arabidopsis *psbA* correlates with RNA structure alterations at the translation

initiation region. *Cells* **10** (2021).

59. M. A. Godoy Herz, M. G. Kubaczka, G. Brzyżek, L. Servi, M. Krzyszton, C. Simpson, J. Brown, S. Swiezewski, E. Petrillo, A. R. Kornblihtt, Light regulates plant alternative splicing through the control of transcriptional elongation. *Mol. Cell* **73**, 1066–1074.e3 (2019).

60. X. Zhao, J. Huang, J. Chory, Unraveling the linkage between retrograde signaling and RNA metabolism in plants. *Trends Plant Sci.* **25**, 141–147 (2020).

61. X. Fang, G. Zhao, S. Zhang, Y. Li, H. Gu, Y. Li, Q. Zhao, Y. Qi, Chloroplast-to-nucleus signaling regulates microRNA biogenesis in *Arabidopsis*. *Dev. Cell* **48**, 371–382.e4 (2019).

62. S. Takano, J. Tomita, K. Sonoike, H. Iwasaki, The initiation of nocturnal dormancy in *Synechococcus* as an active process. *BMC Biol.* **13**, 36 (2015).

63. Y. Seino, T. Takahashi, Y. Hihara, The response regulator RpaB binds to the upstream element of photosystem I genes to work for positive regulation under low-light conditions in *Synechocystis* sp. strain PCC 6803. *J. Bacteriol.* **191**, 1581–1586 (2009).

64. R. Rachedi, M. Foglino, A. Latifi, Stress signaling in cyanobacteria: a mechanistic overview. *Life* **10** (2020).

65. R. D. Hood, S. A. Higgins, A. Flamholz, R. J. Nichols, D. F. Savage, The stringent response regulates adaptation to darkness in the cyanobacterium *Synechococcus elongatus*. *Proc. Natl. Acad. Sci. U. S. A.* **113**, E4867–76 (2016).

66. P. Shah, Y. Ding, M. Niemczyk, G. Kudla, J. B. Plotkin, Rate-limiting steps in yeast protein translation. *Cell* **153**, 1589–1601 (2013).

67. T. Morisaki, K. Lyon, K. F. DeLuca, J. G. DeLuca, B. P. English, Z. Zhang, L. D. Lavis, J. B. Grimm, S. Viswanathan, L. L. Looger, T. Lionnet, T. J. Stasevich, Real-time quantification of single RNA translation dynamics in living cells. *Science* **352**, 1425–1429 (2016).

68. B. Wu, C. Eliscovich, Y. J. Yoon, R. H. Singer, Translation dynamics of single mRNAs in live cells and neurons. *Science* **352**, 1430–1435 (2016).

69. X. Yan, T. A. Hoek, R. D. Vale, M. E. Tanenbaum, Dynamics of translation of single mRNA molecules *in vivo*. *Cell* **165**, 976–989 (2016).

70. C. Wang, B. Han, R. Zhou, X. Zhuang, Real-time imaging of translation on single mRNA transcripts in live cells. *Cell* **165**, 990–1001 (2016).

71. A. Riba, N. Di Nanni, N. Mittal, E. Arhné, A. Schmidt, M. Zavolan, Protein synthesis rates and ribosome occupancies reveal determinants of translation elongation rates. *Proc. Natl. Acad. Sci. U. S. A.* **116**, 15023–15032 (2019).

72. N. M. Livingston, J. Kwon, O. Valera, J. A. Saba, N. K. Sinha, P. Reddy, B. Nelson, C. Wolfe, T. Ha, R. Green, J. Liu, B. Wu, Bursting translation on single mRNAs in live cells. *Mol. Cell* **83**, 2276–2289.e11 (2023).

73. K. Nakahigashi, Y. Takai, Y. Shiwa, M. Wada, M. Honma, H. Yoshikawa, M. Tomita, A. Kanai, H. Mori, Effect of codon adaptation on codon-level and gene-level translation efficiency *in vivo*. *BMC Genomics* **15**, 1115 (2014).

74. D. E. Weinberg, P. Shah, S. W. Eichhorn, J. A. Hussmann, J. B. Plotkin, D. P. Bartel, Improved ribosome-footprint and mRNA measurements provide insights into dynamics and regulation of yeast translation. *Cell Rep.* **14**, 1787–1799 (2016).

75. D. D. Erdmann-Pham, K. Dao Duc, Y. S. Song, The key parameters that govern translation efficiency. *Cell Syst* **10**, 183–192.e6 (2020).

76. J. Kim, P. G. Klein, J. E. Mullet, Ribosomes pause at specific sites during synthesis of membrane-bound chloroplast reaction center protein D1. *J. Biol. Chem.* **266**, 14931–14938 (1991).

77. J. Kim, P. G. Klein, J. E. Mullet, Synthesis and turnover of photosystem II reaction center protein D1. Ribosome pausing increases during chloroplast development. *J. Biol. Chem.* **269**, 17918–17923 (1994).

78. N. R. Guydosh, R. Green, Dom34 rescues ribosomes in 3′ untranslated regions. *Cell* **156**, 950–962 (2014).

79. A. B. Arpat, A. Liechti, M. De Matos, R. Dreos, P. Janich, D. Gatfield, Transcriptome-wide sites of collided ribosomes reveal principles of translational pausing. *Genome Res.* **30**, 985–999 (2020).

80. S. Meydan, N. R. Guydosh, Disome and trisome profiling reveal genome-wide targets of ribosome quality control. *Mol. Cell* **79**, 588–602.e6 (2020).

81. T. Zhao, Y. M. Chen, Y. Li, J. Wang, S. Chen, N. Gao, W. Qian, Disome-seq reveals widespread ribosome collisions that promote cotranslational protein folding. *Genome Biol.* **22**, 16 (2021).

82. L. Provasoli, Artificial media for fresh water algae: problems and suggestions. *The ecology of algae* **2**, 84–96 (1960).

83. R. Rippka, R. Y. Stanier, J. Deruelles, M. Herdman, J. B. Waterbury, Generic assignments, strain histories and properties of pure cultures of cyanobacteria. *Microbiology* **111**, 1–61 (1979).

84. M. Mito, Y. Mishima, S. Iwasaki, Protocol for disome profiling to survey ribosome collision in humans and zebrafish. *STAR Protoc* **1**, 100168 (2020).

85. T. Fujita, T. Yokoyama, M. Shirouzu, H. Taguchi, T. Ito, S. Iwasaki, The landscape of translational stall sites in bacteria revealed by monosome and disome profiling. *RNA* **28**, 290–302 (2022).

86. K. Kashiwagi, Y. Shichino, T. Osaki, A. Sakamoto, M. Nishimoto, M. Takahashi, M. Mito, F. Weber, Y. Ikeuchi, S. Iwasaki, T. Ito, eIF2B-capturing viral protein NSs suppresses the integrated stress response. *Nat. Commun.* **12**, 7102 (2021).

87. S. Chen, Y. Zhou, Y. Chen, J. Gu, fastp: an ultra-fast all-in-one FASTQ preprocessor. *Bioinformatics* **34**, i884–i890 (2018).

88. A. Dobin, C. A. Davis, F. Schlesinger, J. Drenkow, C. Zaleski, S. Jha, P. Batut, M. Chaisson, T. R. Gingeras, STAR: ultrafast universal RNA-seq aligner. *Bioinformatics* **29**, 15–21 (2013).

89. B. Langmead, S. L. Salzberg, Fast gapped-read alignment with Bowtie 2. *Nat. Methods* **9**, 357–359 (2012).

90. M. I. Love, W. Huber, S. Anders, Moderated estimation of fold change and

dispersion for RNA-seq data with DESeq2. *Genome Biol.* **15**, 550 (2014).

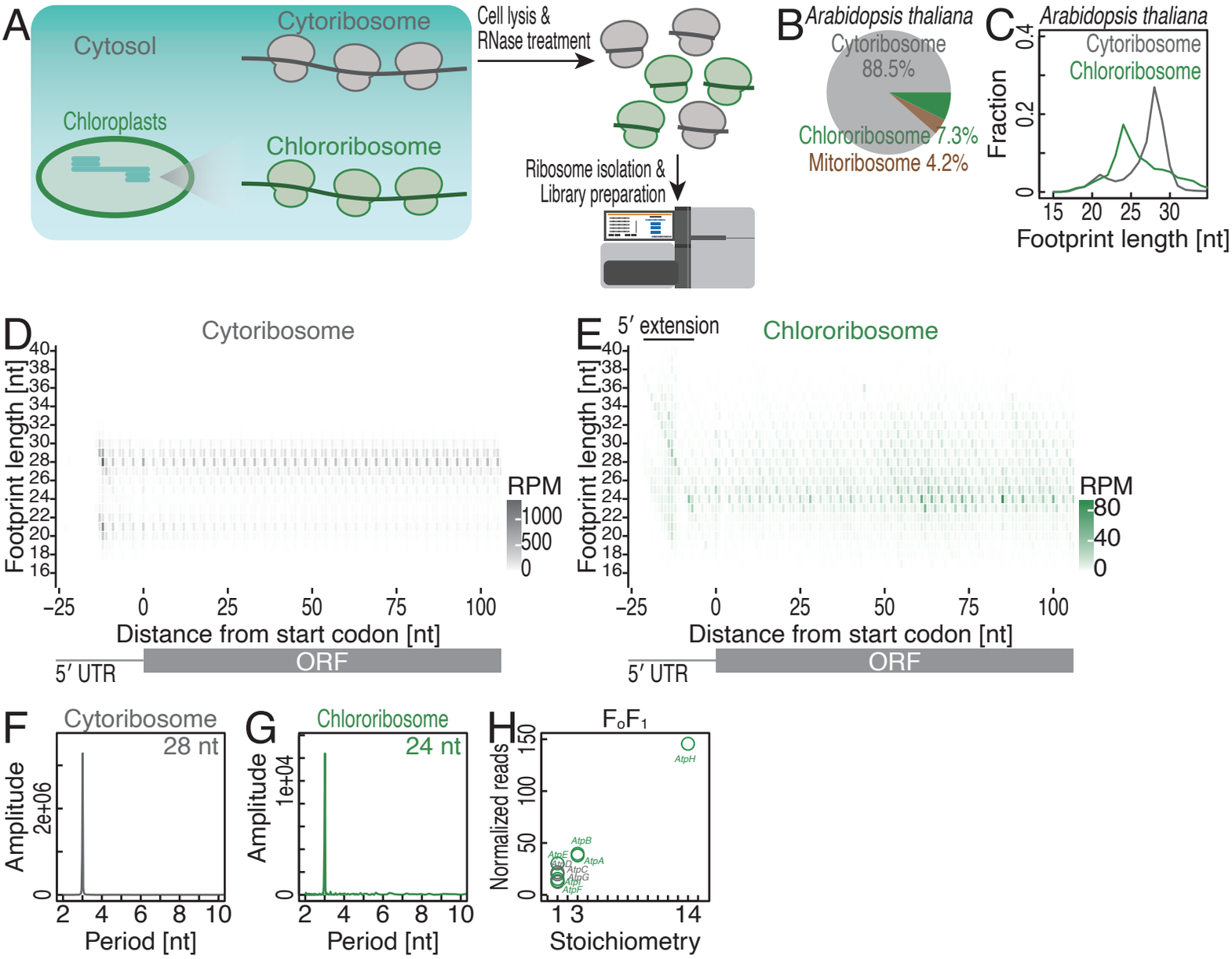

Figure 1 Fujita Wakigawa *et al.* (2024)

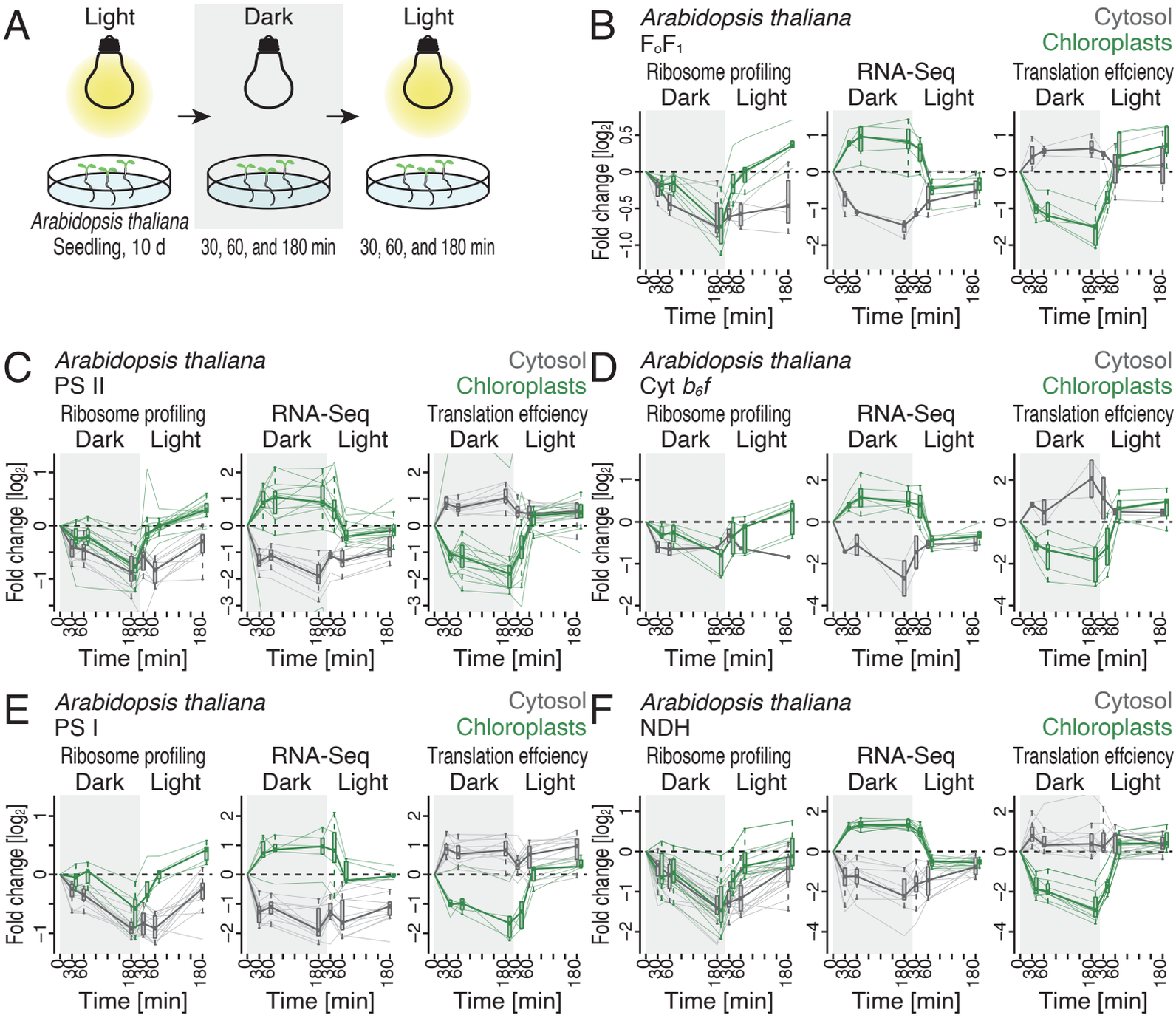

Figure 2 Fujita, Wakigawa *et al.* (2024)

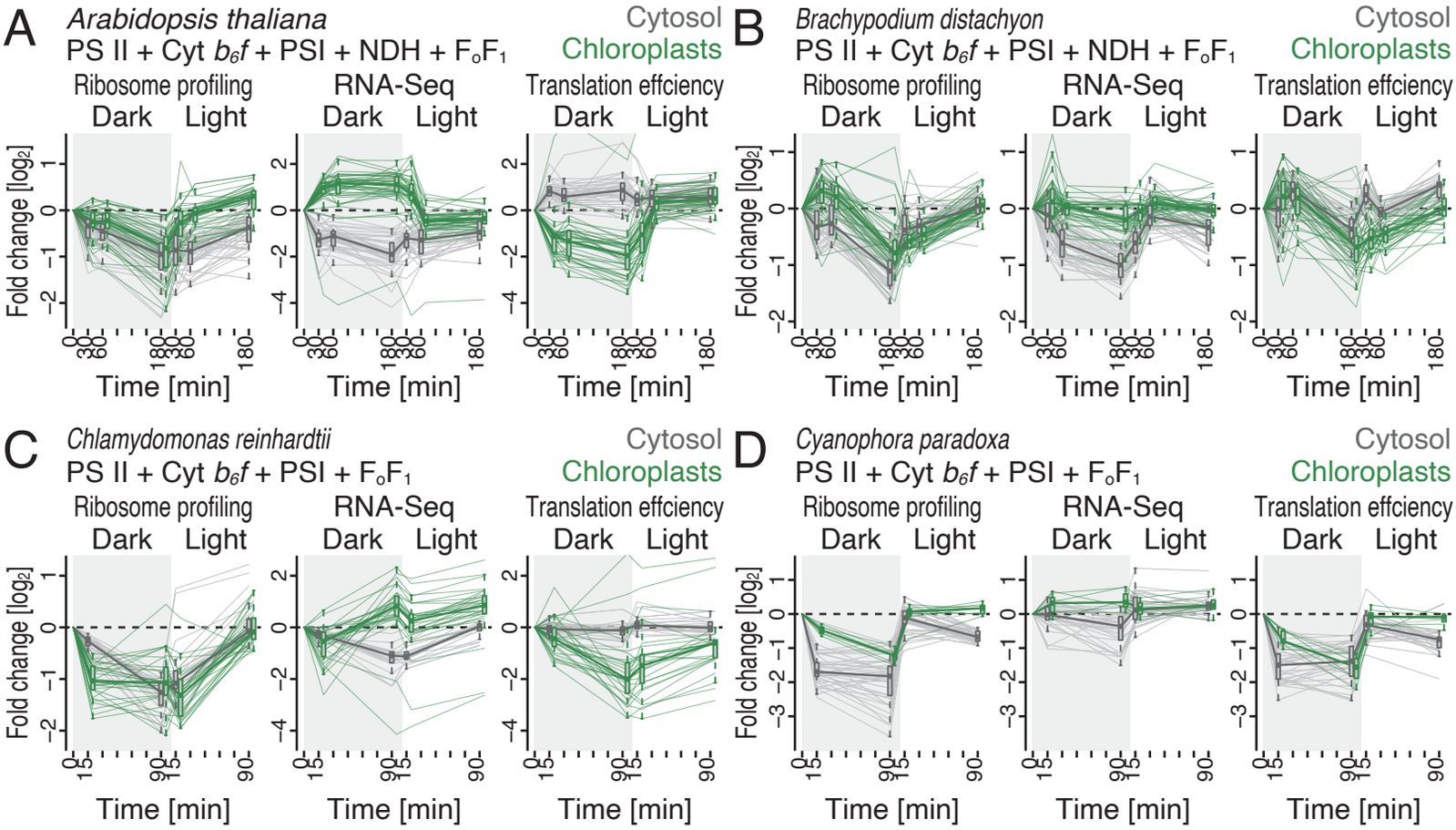

Figure 3 Fujita, Wakigawa *et al.* (2024)

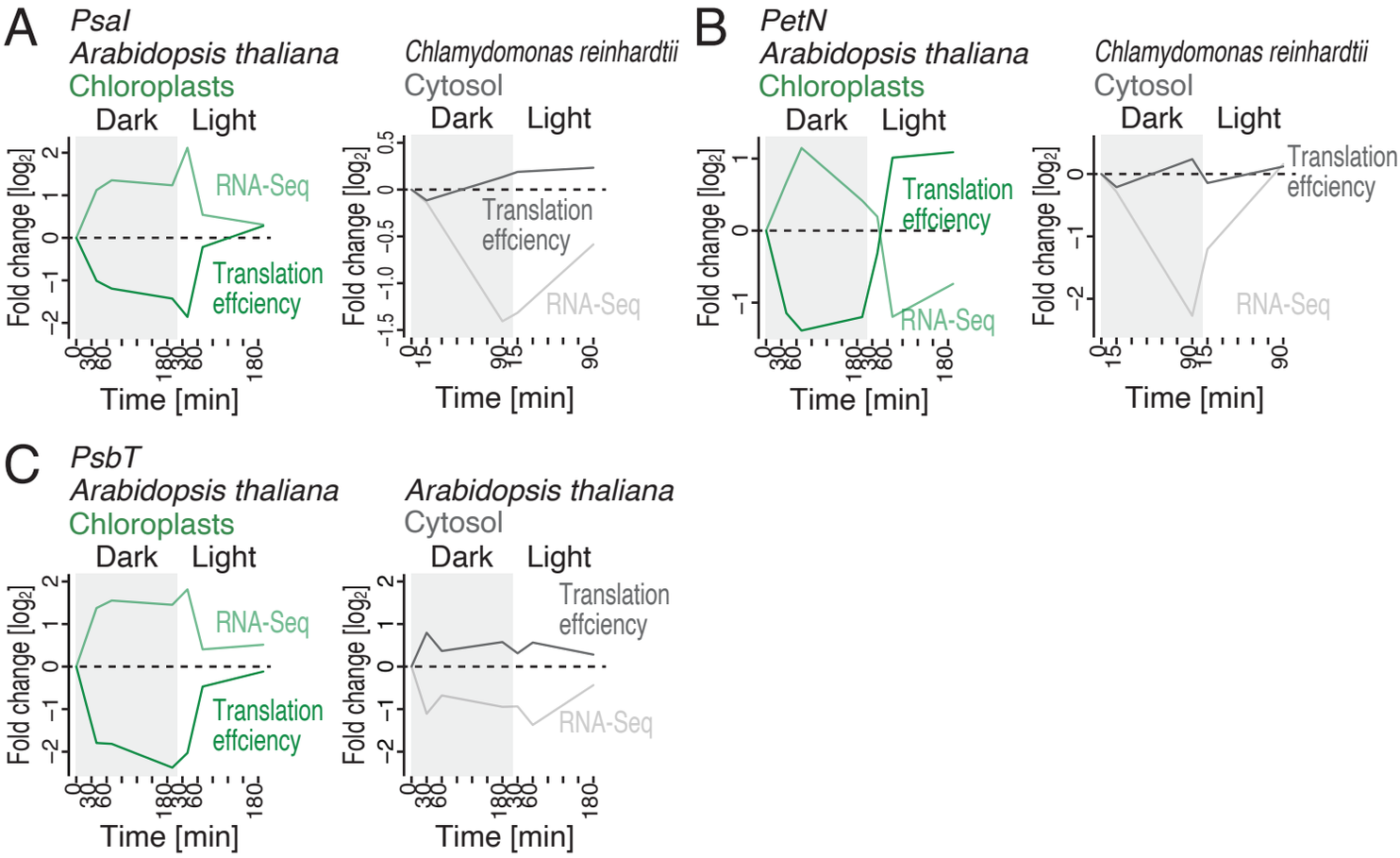

Figure 4 Fujita, Wakigawa *et al.* (2024)

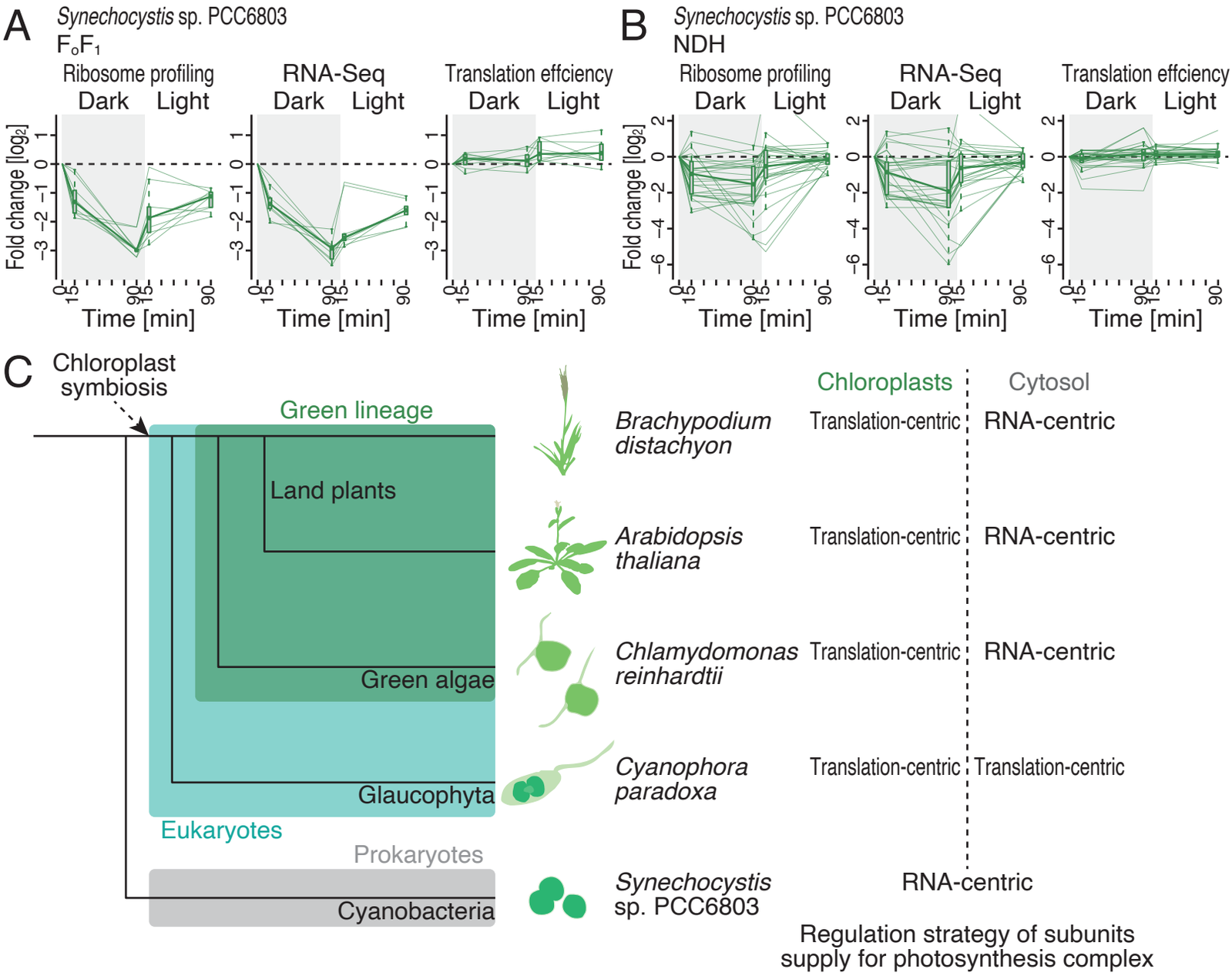

Figure 5 Fujita, Wakigawa *et al.* (2024)

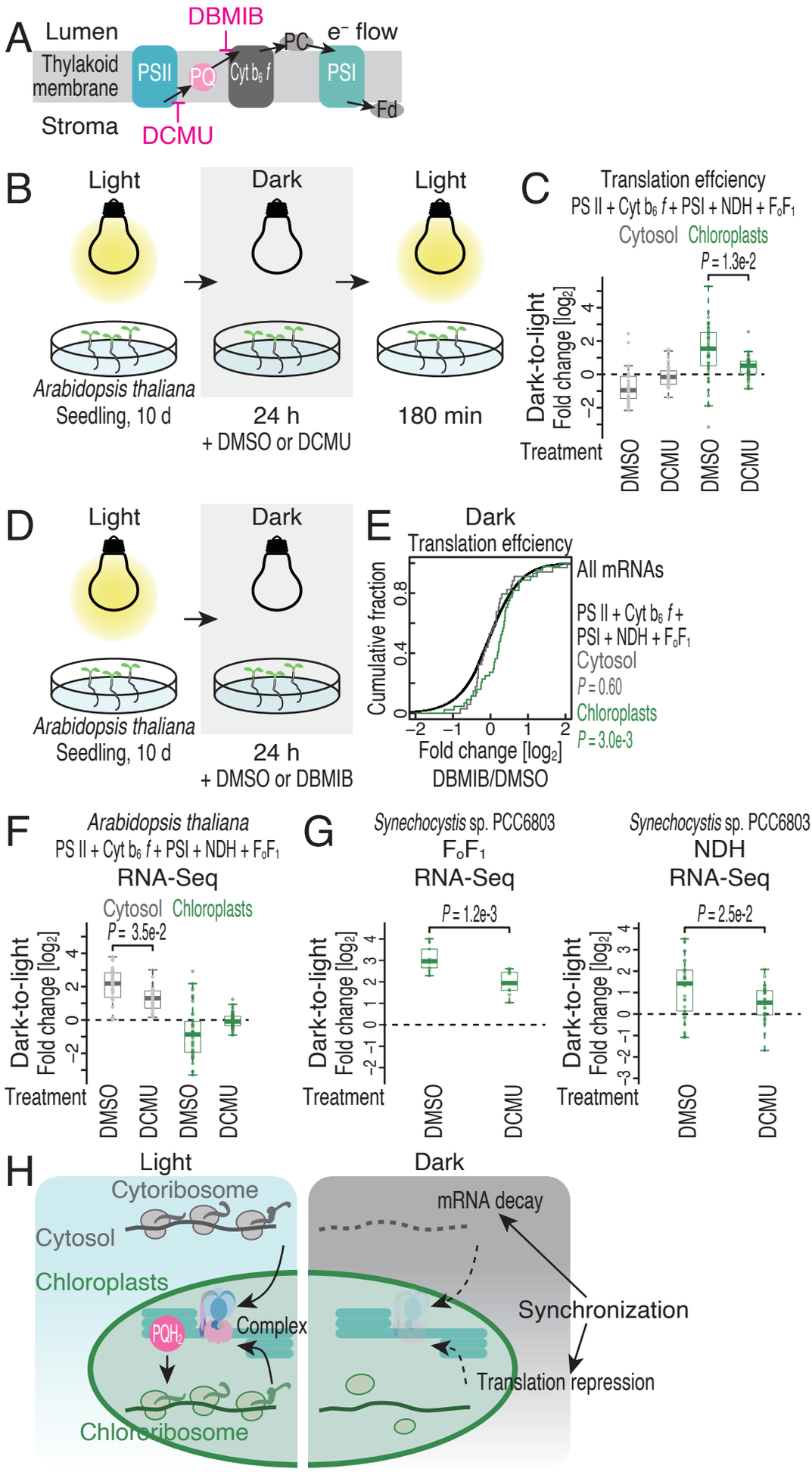

Figure 6 Fujita, Wakigawa *et al.* (2024)

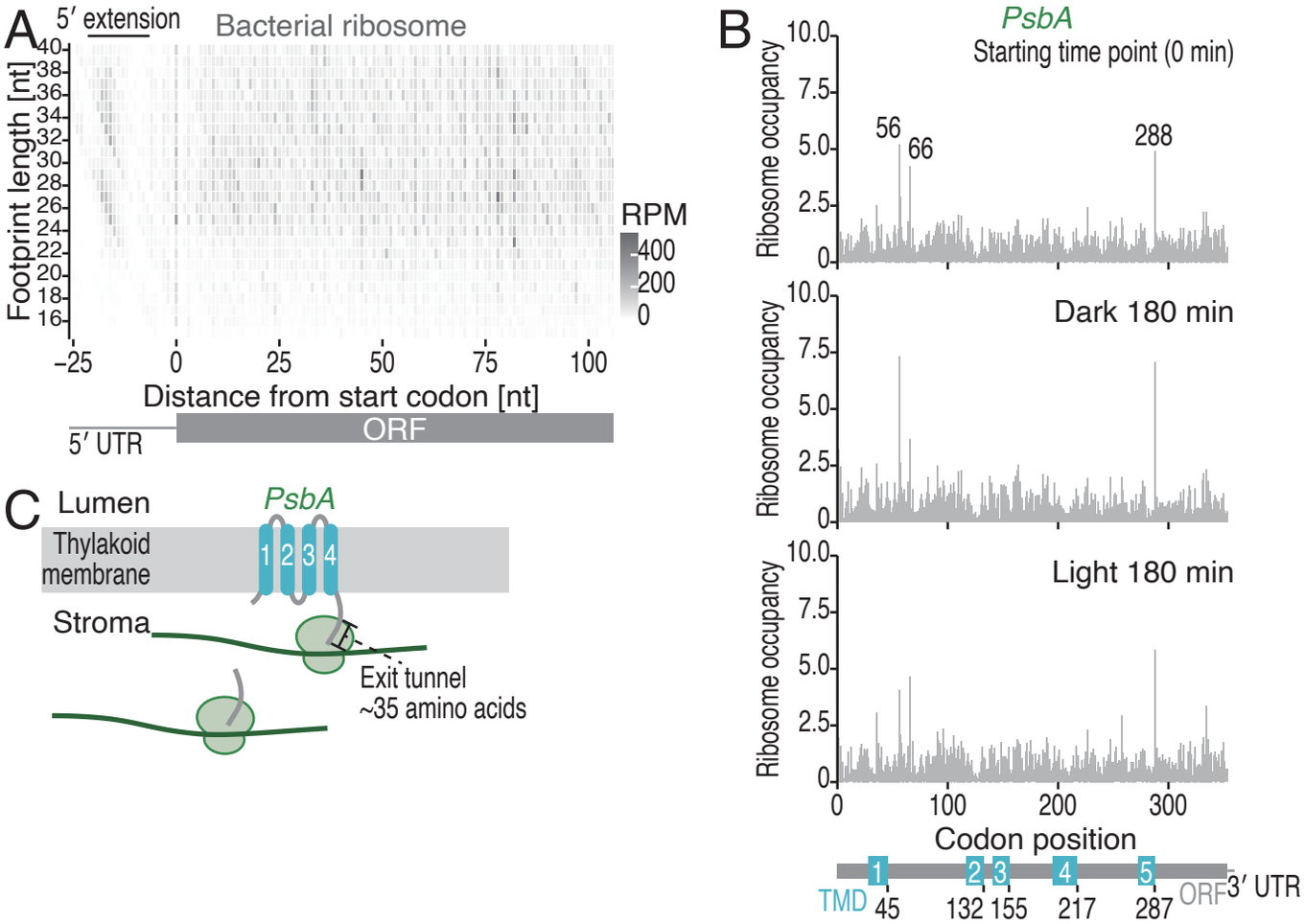

Figure S1 Fujita, Wakigawa *et al.* (2024)

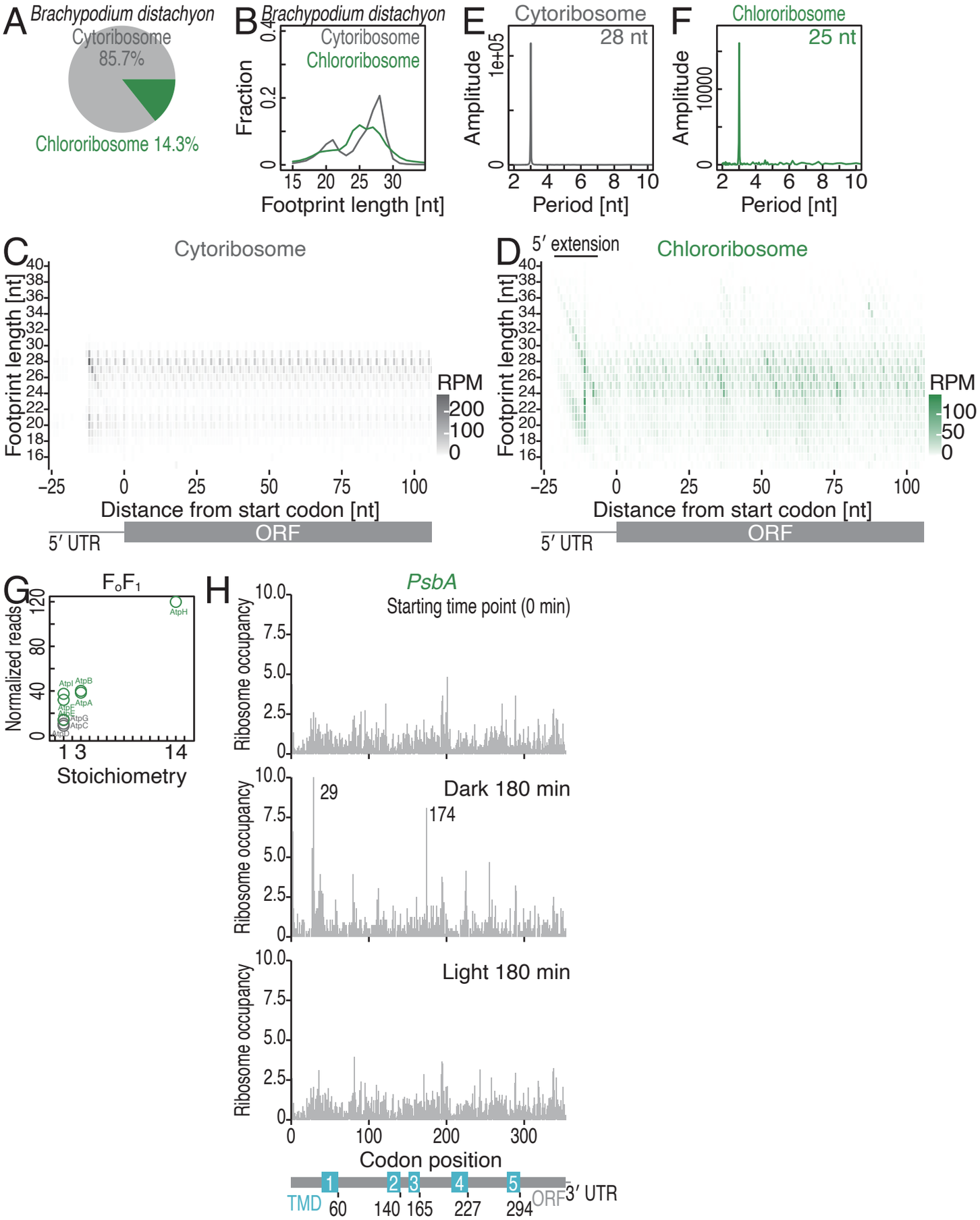

Figure S2 Fujita, Wakigawa *et al.* (2024)

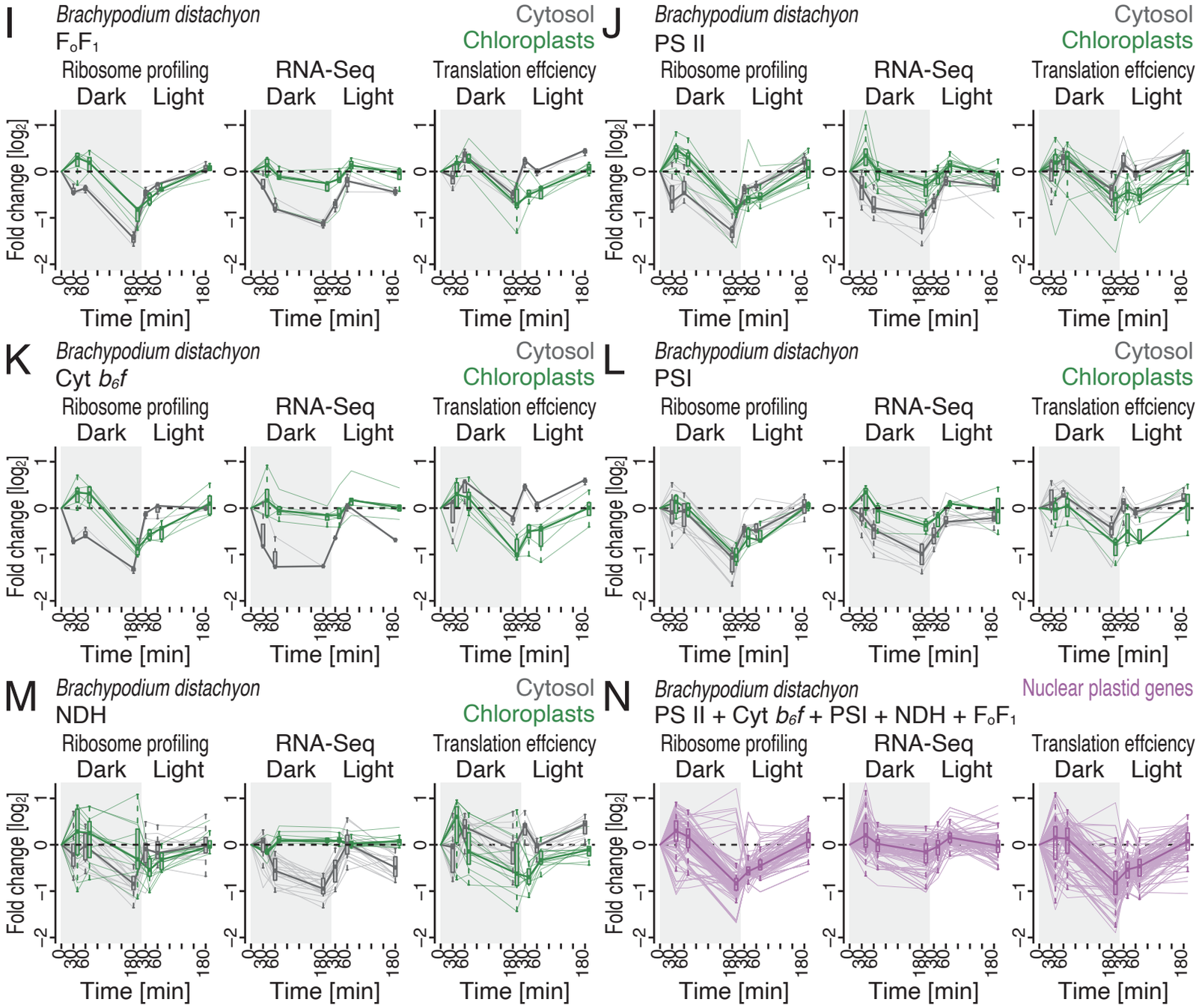

Figure S2 Fujita, Wakigawa *et al.* (2024)

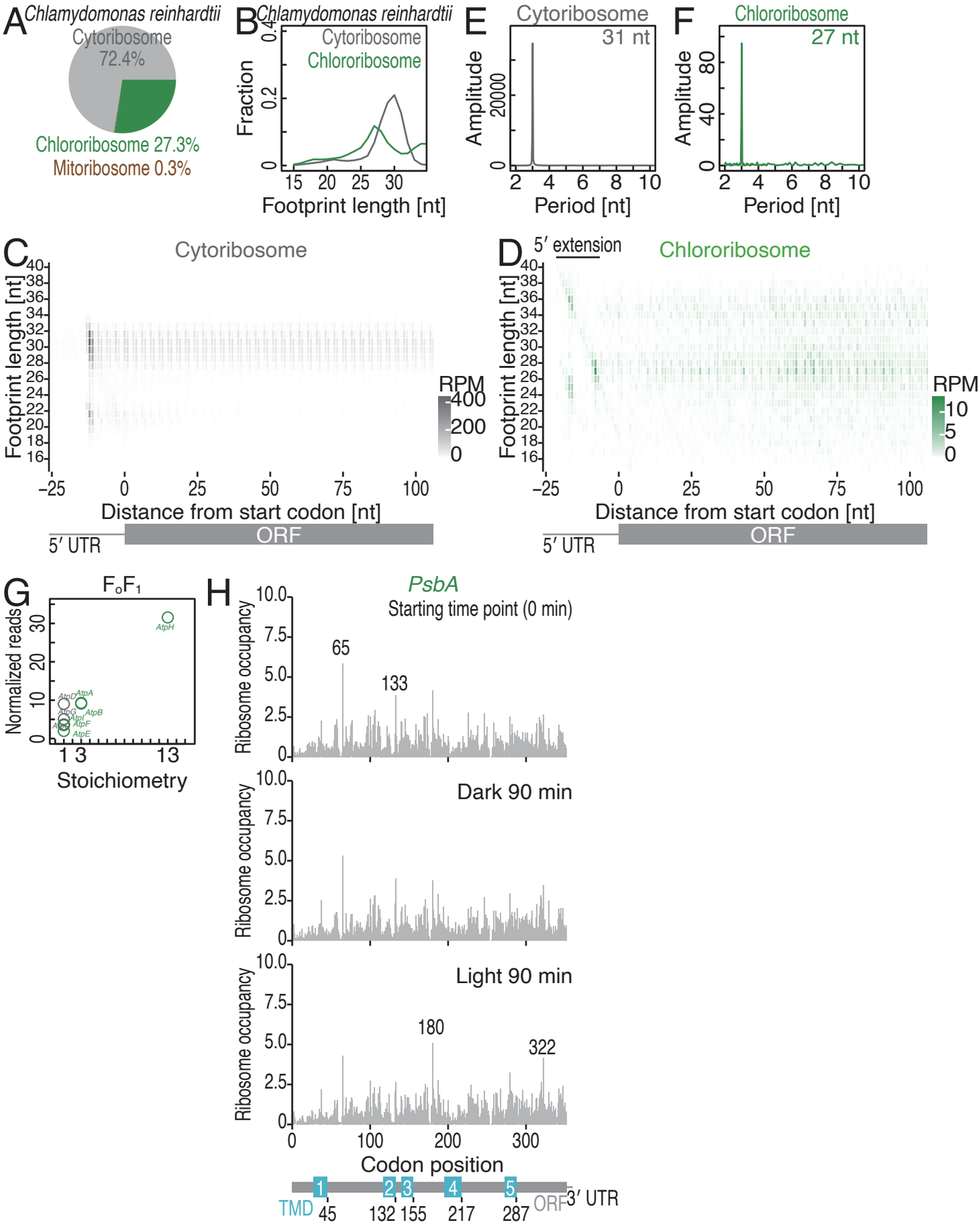

Figure S3 Fujita, Wakigawa *et al.* (2024)

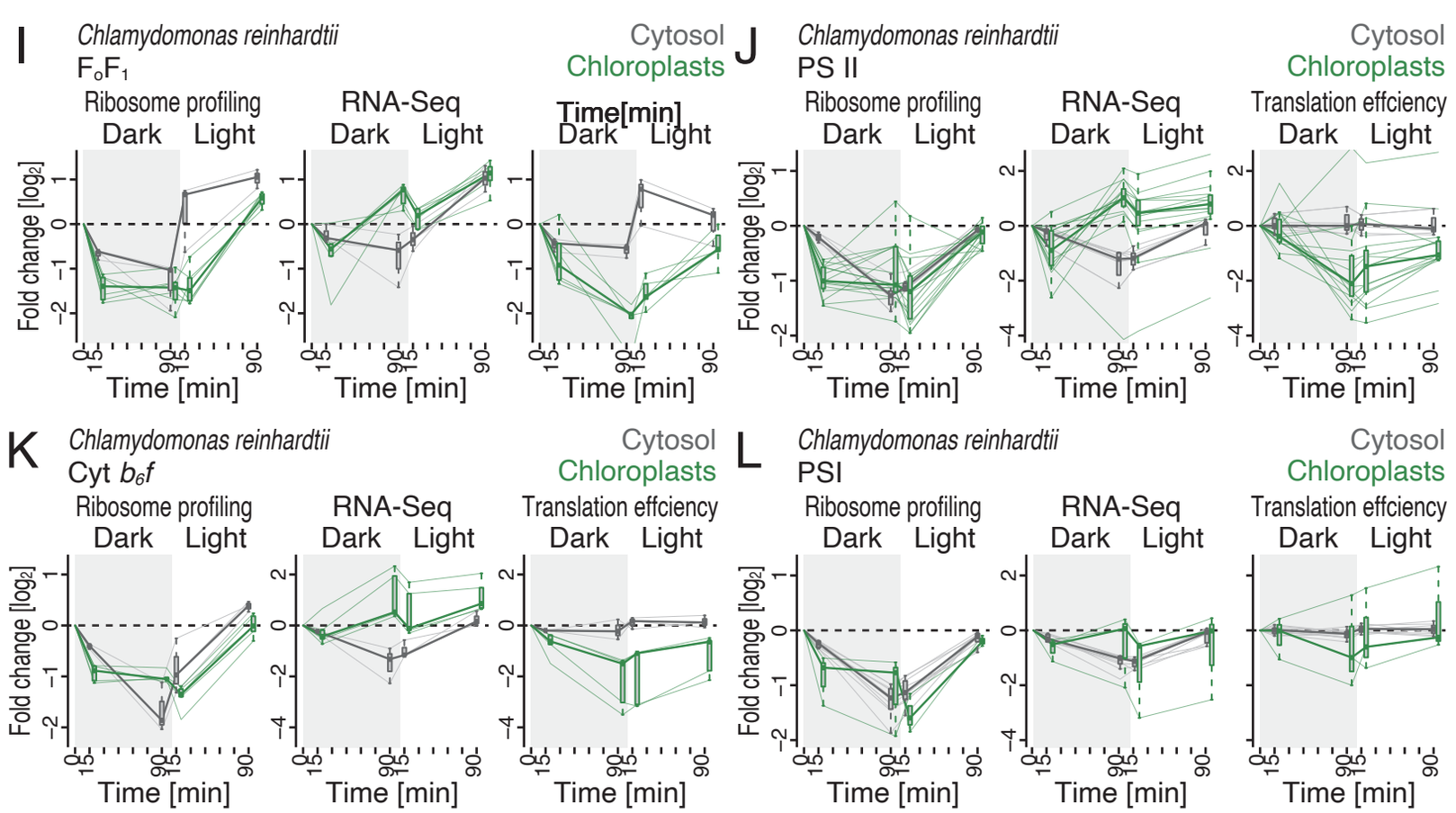

Figure S3 Fujita, Wakigawa *et al.* (2024)

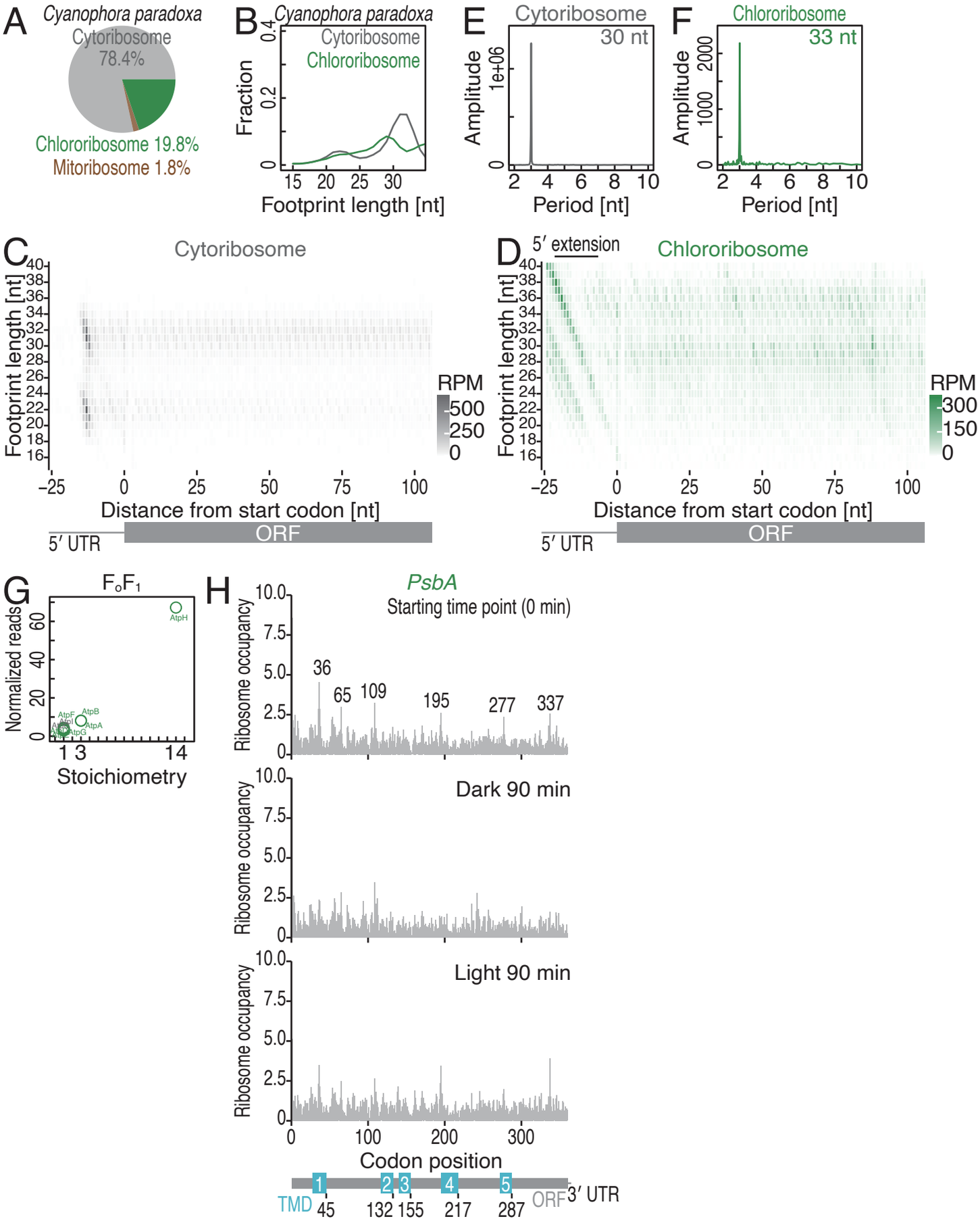

Figure S4 Fujita, Wakigawa *et al.* (2024)

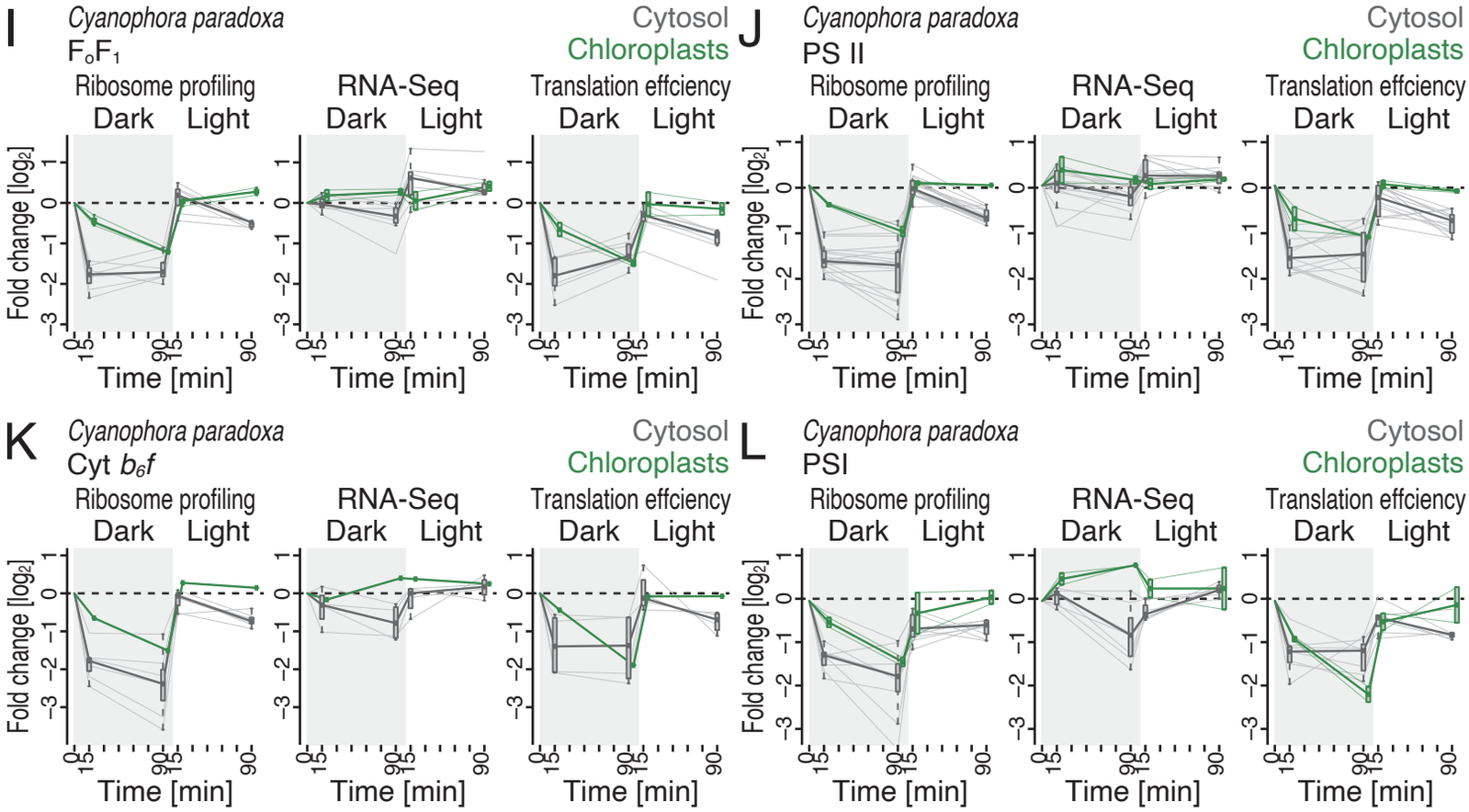

Figure S4 Fujita, Wakigawa *et al.* (2024)

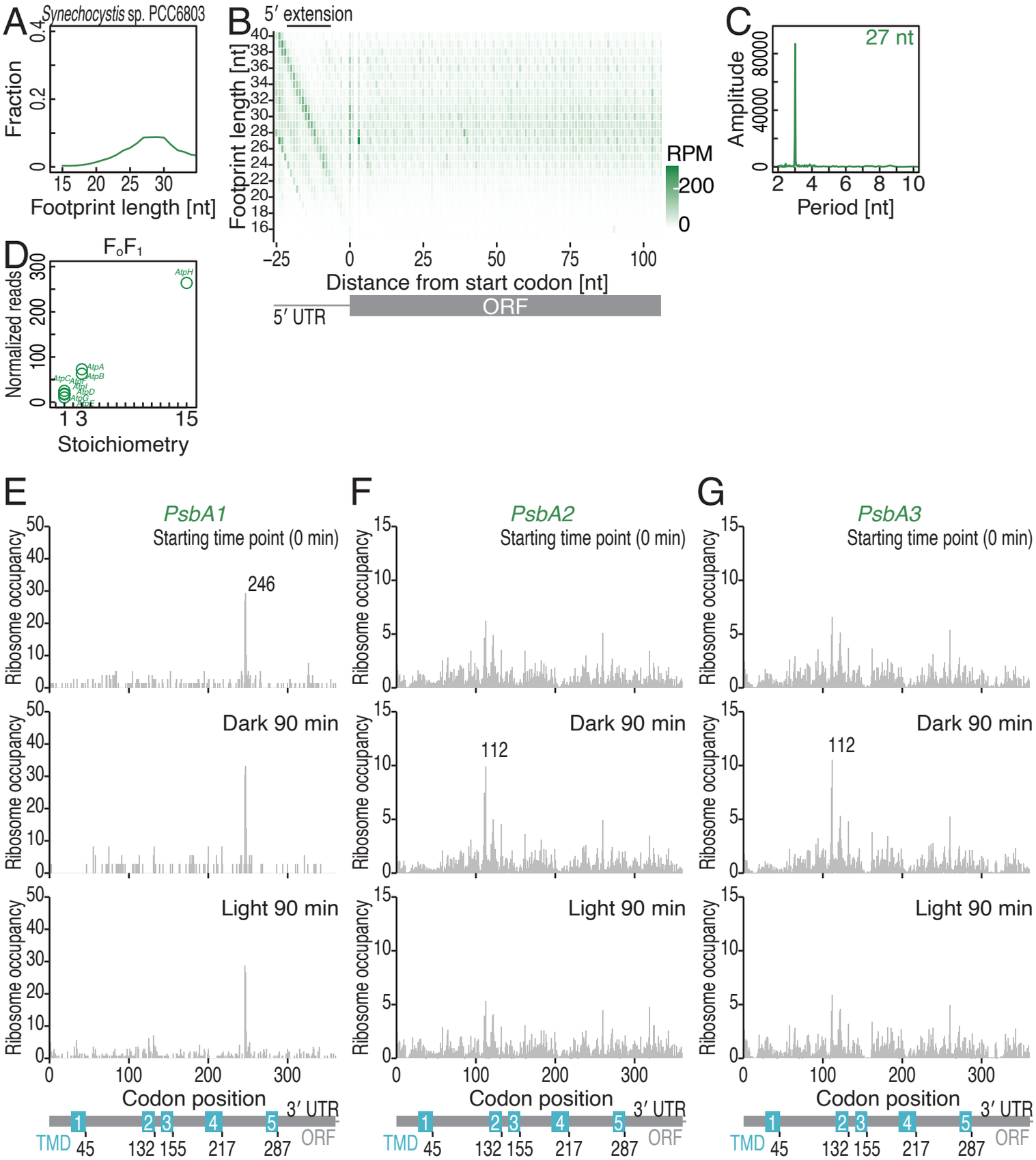

Figure S5 Fujita, Wakigawa *et al.* (2024)

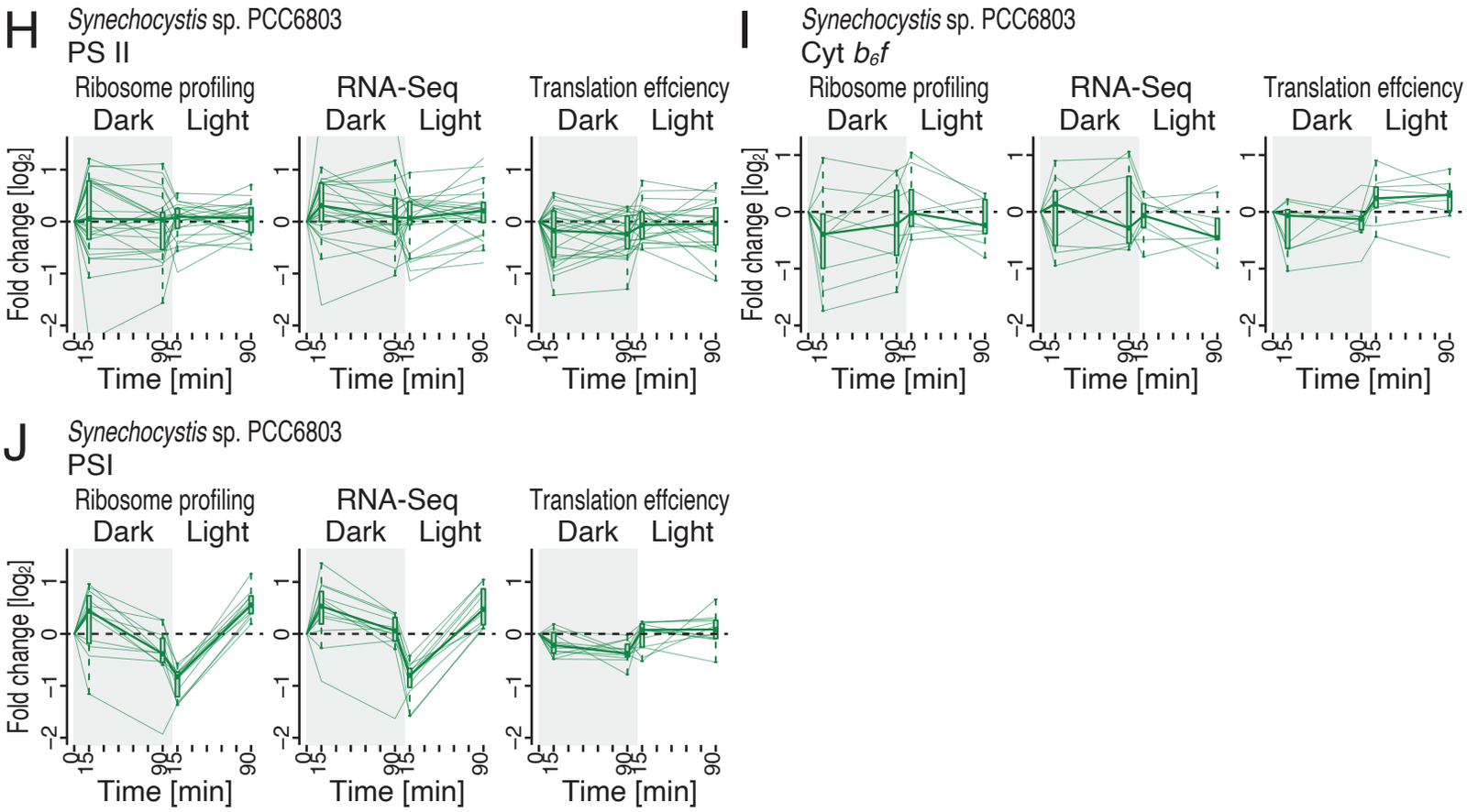

Figure S5 Fujita, Wakigawa *et al.* (2024)

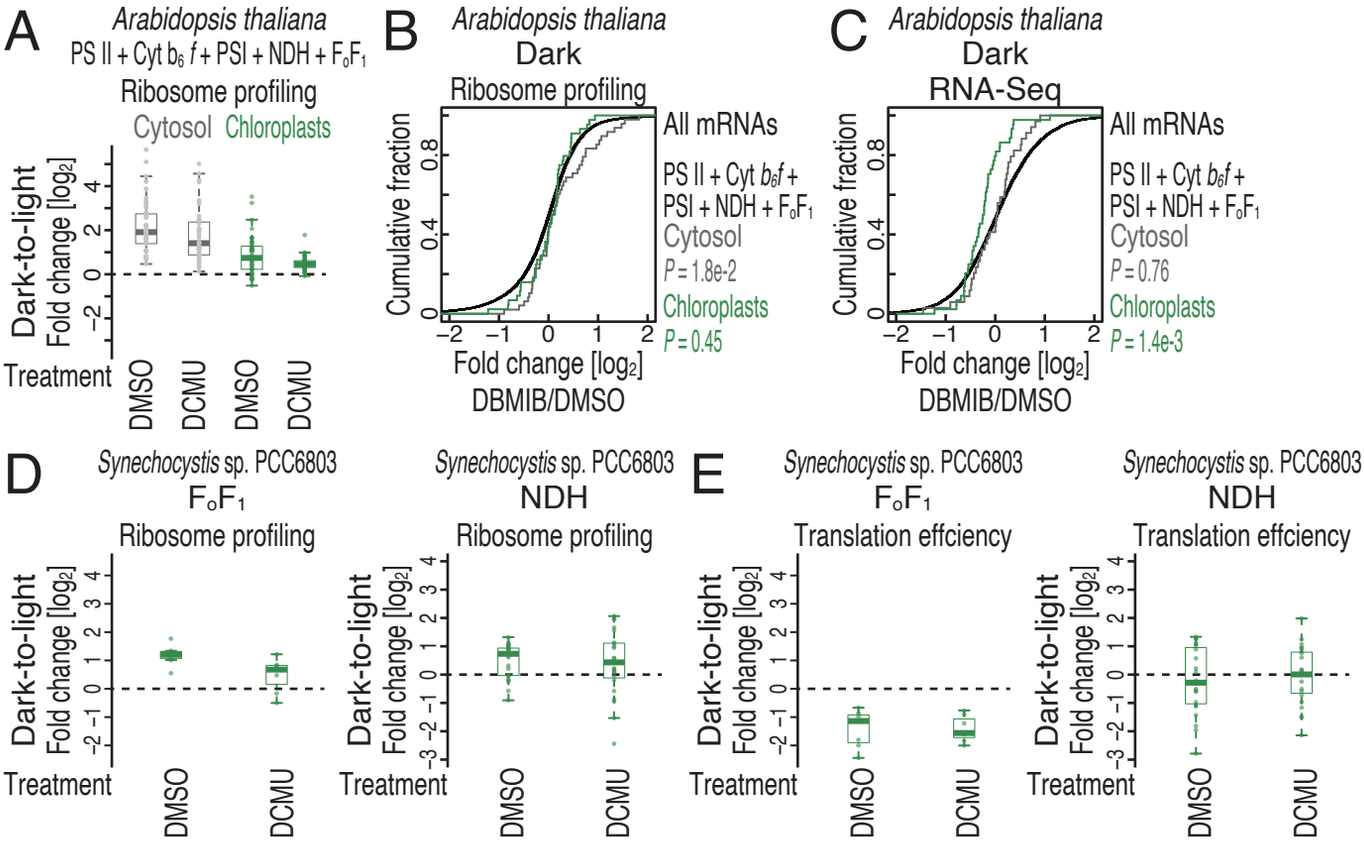

Figure S6 Fujita, Wakigawa *et al.* (2024)